Resonating neurons stabilize heterogeneous grid-cell networks

Divyansh Mittal and Rishikesh Narayanan*

Cellular Neurophysiology Laboratory, Molecular Biophysics Unit, Indian Institute of Science, Bangalore, India.

***Corresponding Author**

Rishikesh Narayanan, Ph.D.
Molecular Biophysics Unit
Indian Institute of Science
Bangalore 560 012, India.

e-mail: rishi@iisc.ac.in
Phone: +91-80-22933372
Fax: +91-80-23600535

Number of words: 250 (abstract), 120 (significance statement)

Abbreviated title: Resonating neurons stabilize heterogeneous networks

Keywords: grid cells, entorhinal cortex, continuous attractor network, resonance, heterogeneities

Author contributions
D. M. and R. N. designed experiments; D. M. performed experiments and carried out data analysis; D. M. and R. N. co-wrote the paper.

Competing financial interests
The authors declare no conflict of interest.

Acknowledgments

This work was supported by the Wellcome Trust-DBT India Alliance (Senior fellowship to RN; IA/S/16/2/502727), Human Frontier Science Program (HFSP) Organization (RN), the Department of Biotechnology through the DBT-IISc partnership program (RN), the Revati and Satya Nadham Atluri Chair Professorship (RN), and the Ministry of Human Resource Development (RN & DM). The authors thank Dr. Poonam Mishra, Dr. Sufyan Ashhad and the members of the cellular neurophysiology laboratory for helpful discussions and for comments on a draft of this manuscript. The authors thank Dr. Ila Fiete for helpful discussions.

ABSTRACT

Grid cells in the medial entorhinal cortex manifest multiple firing fields, patterned to tessellate external space with triangles. Although two-dimensional continuous attractor network (CAN) models have offered remarkable insights about grid-patterned activity generation, their functional stability in the presence of biological heterogeneities remains unexplored. In this study, we systematically incorporated three distinct forms of intrinsic and synaptic heterogeneities into a rate-based CAN model driven by virtual trajectories, developed here to mimic animal traversals and improve computational efficiency. We found that increasing degrees of biological heterogeneities progressively disrupted the emergence of grid-patterned activity and resulted in progressively large perturbations in neural activity. Quantitatively, grid score and spatial information associated with neural activity reduced progressively with increasing degree of heterogeneities, and perturbations were primarily confined to low-frequency neural activity. We postulated that suppressing low-frequency perturbations could ameliorate the disruptive impact of heterogeneities on grid-patterned activity. To test this, we formulated a strategy to introduce intrinsic neuronal resonance, a physiological mechanism to suppress low-frequency activity, in our rate-based neuronal model by incorporating filters that mimicked resonating conductances. We confirmed the emergence of grid-patterned activity in homogeneous CAN models built with resonating neurons and assessed the impact of heterogeneities on these models. Strikingly, CAN models with resonating neurons were resilient to the incorporation of heterogeneities and exhibited stable grid-patterned firing, through suppression of low-frequency components in neural activity. Our analyses suggest a universal role for intrinsic neuronal resonance, an established mechanism in biological neurons to suppress low-frequency neural activity, in stabilizing heterogeneous network physiology.

SIGNIFICANCE STATEMENT

A central theme that governs the functional design of biological networks is their ability to sustain stable function despite widespread parametric variability. However, several theoretical and modeling frameworks employ unnatural homogeneous networks in assessing network function owing to the enormous analytical or computational costs involved in assessing heterogeneous networks. Here, we investigate the impact of biological heterogeneities on a powerful two-dimensional continuous attractor network implicated in the emergence of patterned neural activity. We show that network function is disrupted by biological heterogeneities, but is stabilized by intrinsic neuronal resonance, a physiological mechanism that suppresses low-frequency perturbations. As low-frequency perturbations are pervasive across biological systems, mechanisms that suppress low-frequency components could form a generalized route to stabilize heterogeneous biological networks.

INTRODUCTION

Stability of network function, defined as the network's ability to elicit robust functional outcomes despite perturbations to or widespread variability in its constitutive components, is a central theme that governs the functional design of several biological networks. Biological systems exhibit ubiquitous parametric variability spanning different scales of organization, quantified through statistical heterogeneities in the underlying parameters. Strikingly, in spite of such large-scale heterogeneities, outputs of biological networks are stable, and are precisely tuned to meet physiological demands. A central question that spans different scales of organization is on the ability of biological networks to achieve physiological stability in the face of ubiquitous parametric variability (1-11).

Biological heterogeneities are known to play critical roles in governing stability of network function, through intricate and complex interactions among mechanisms underlying functional emergence (8, 9, 11-29). However, an overwhelming majority of theoretical and modeling frameworks lack the foundation to evaluate the impact of such heterogeneities on network output, as they employ unnatural homogeneous networks in assessing network function. The paucity of heterogeneous network frameworks is partly attributable to the enormous analytical or computational costs involved in assessing heterogeneous networks. In this study, we quantitatively address questions on the impact of distinct forms of biological heterogeneities on the functional stability of a two-dimensional continuous attractor network (CAN), which has been implicated in the generation of patterned neuronal activity in grid cells of the medial entorhinal cortex (30-36). Although the continuous attractor framework has offered insights about information encoding across several neural circuits (27, 30, 34, 36-48), the fundamental question on the stability of 2-D CAN models in the presence of biological heterogeneities remains unexplored. Here, we systematically assessed the impact of biological heterogeneities on stability of emergent spatial representations in a 2-D CAN model, and unveiled a physiologically plausible neural mechanism that promotes stability despite the expression of heterogeneities.

We first developed an algorithm to generate virtual trajectories that closely mimicked animal traversals in an open arena, to provide better computational efficiency in terms of covering the entire arena within shorter time duration. We employed these virtual trajectories to drive a rate-based homogeneous CAN model that elicited grid-patterned neural activity (30), and systematically introduced different degrees of three distinct forms of biological heterogeneities. The three distinct forms of biological heterogeneities that we introduced, either individually or together, were in neuronal intrinsic properties, in afferent inputs

carrying behavioral information and in local-circuit synaptic connectivity. We found that the incorporation of these different forms of biological heterogeneities disrupted the emergence of grid-patterned activity by introducing perturbations in neural activity, predominantly in low-frequency components. In the default model where neurons were integrators, grid-patterns and spatial information in neural activity were progressively lost with increasing degrees of biological heterogeneities, and were accompanied by progressive increases in low-frequency perturbations.

As heterogeneity-induced perturbations to neural activity were predominantly in the lower frequencies, we postulated that suppressing low-frequency perturbations could ameliorate the disruptive impact of biological heterogeneities on grid-patterned activity. We recognized intrinsic neuronal resonance as an established biological mechanism that suppresses low-frequency components, effectuated by the expression of resonating conductances endowed with specific biophysical characteristics (49-54). Consequently, we hypothesized that intrinsic neuronal resonance could stabilize the heterogeneous grid-cell network through suppression of low-frequency perturbations. To test this hypothesis, we developed a strategy to introduce intrinsic resonance in our rate-based neuronal model by incorporating an additional tunable high-pass filter that mimicked the function of resonating conductances in biological neurons. We confirmed that the emergence of grid-patterned activity was not affected by replacing all the integrator neurons in the homogeneous CAN model with theta-frequency resonators. We systematically incorporated different forms of biological heterogeneities into the 2-D resonator CAN model and found that intrinsic neuronal resonance stabilized heterogeneous neural networks, through suppression of low-frequency components of neural activity. Together, our study unveils an important role for intrinsic neuronal resonance in stabilizing network physiology through the suppression of heterogeneity-induced perturbations in low-frequency components of network activity. As the dominance of low-frequency perturbations is pervasive across biological networks (55-59), we postulate that mechanisms that suppress low-frequency components could be a generalized route to stabilize heterogeneous biological networks.

RESULTS

The rate-based CAN model with the default integrator neurons for eliciting grid cell activity was adopted from Burak and Fiete (30). The CAN model consisted of a 2D neural sheet, composed of 60×60 = 3600 neurons in the default network. The sides of this neural sheet were connected, yielding a toroidal (or periodic) network configuration. Each neuron in the CAN model received two distinct sets of synaptic inputs, one from other neurons within the network and another feed-forward afferent input that was dependent on the velocity of the virtual animal. The movement of the virtual animal was modeled to occur in a circular 2D spatial arena (Fig. 1*A*; *Real trajectory*), and was simulated employing recordings of rat movement (60) to replicate earlier results (30). However, the real trajectory spanned 590 s of real-world time and required considerable simulation time to sufficiently explore the entire arena, essential for computing high-resolution spatial activity maps. Consequently, the computational costs required for exploring the parametric space of the CAN model, with different forms of network heterogeneities in networks of different sizes and endowed with distinct kinds of neurons, were exorbitant. Therefore, we developed a virtual trajectory, mimicking smooth animal movement within the arena, but with sharp turns at the borders.

Our analyses demonstrated the ability of virtual trajectories to cover the entire arena with lesser time (Fig. 1*A*; *Virtual trajectory*), while not compromising on the accuracy of the spatial activity maps constructed from this trajectory in comparison to the maps obtained with the real trajectory (Fig. 1*B*, Fig S1). Specifically, the correlation values between the spatial autocorrelation of rate maps of individual grid cells for real trajectory and that from the virtual trajectory at different rat runtimes (T_{run}) were high across all measured runtimes (Fig. 1*B*). These correlation values showed a saturating increase with increase in T_{run}. As there was no substantial improvement in accuracy beyond T_{run}= 100 s, we employed T_{run}= 100 s for all simulations (compared to the 590 s of the real trajectory). Therefore, our virtual trajectory covered similar areas in ~6 times lesser duration (Fig. 1*A*), which reduced the simulation duration by a factor of ~10 times when compared to the real rat trajectory, while yielding similar spatial activity maps (Fig. 1*B*, Fig S1). Our algorithm also allowed us to generate fast virtual trajectories mimicking rat trajectories in open arenas of different shapes (Circle: Fig. 1*A*; Square: Fig. 2*E*).

Biologically prevalent network heterogeneities disrupted the emergence of grid cell activity in CAN models.

The simulated CAN model (Fig. 1) is an idealized homogeneous network of intrinsically identical neurons, endowed with precise local connectivity patterns and identical response properties for afferent inputs. Although this idealized CAN model provides an effective phenomenological framework to understand and simulate grid cell activity, the underlying network does not account for the ubiquitous biological heterogeneities that span neuronal intrinsic properties and synaptic connectivity patterns. Would the CAN model sustain grid-cell activity in a network endowed with biological heterogeneities in neuronal intrinsic properties and strengths of afferent/local synaptic inputs? If yes, how do different forms of biological heterogeneities, introduced at different degrees, affect grid-cell activity?

To address these questions, we systematically introduced three distinct forms of biological heterogeneities into the rate-based CAN model. We introduced *intrinsic heterogeneity* by randomizing the value of the neuronal integration time constant τ across neurons in the network. Within the rate-based framework employed here, randomization of τ reflected physiological heterogeneities in neuronal excitability properties, and larger spans of τ defined higher degrees of intrinsic heterogeneity (Table S1; Fig. 2*A*). *Afferent heterogeneity* referred to heterogeneities in the coupling of afferent velocity inputs onto individual neurons. Different degrees of afferent heterogeneities were introduced by randomizing the velocity scaling factor (α) in each neuron through uniform distributions of different ranges (Table S1; Fig. 2*B*). S*ynaptic heterogeneity* involved the local connectivity matrix, and was introduced as additive jitter to the default center-surround connectivity matrix. Synaptic jitter was independently sampled for each connection, from a uniform distribution whose differential span regulated the associated higher degree of heterogeneity (Table S1; Fig 2*C*). In homogeneous networks, τ (=10 ms), α (=45) and W_{ij} (center-shifted Mexican hat connectivity without jitter) were identical across all neurons in the network. We assessed four distinct sets of heterogeneous networks: three sets endowed with one of intrinsic, afferent and synaptic heterogeneities, and a fourth where all three forms of heterogeneities were co-expressed. When all heterogeneities were present together, all three sets of parameters were set randomly with the degree of heterogeneity defining the bounds of the associated distribution (Table S1).

We found that the incorporation of any of the three forms of heterogeneities into the CAN model resulted in the disruption of grid pattern formation, with the deleterious impact

increasing with increasing degree of heterogeneity (Fig. 2*E*). Quantitatively, we employed grid score (60, 61) to measure the emergence of pattern formation in the CAN model activity, and found a reduction in grid score with increase in the degree of each form of heterogeneity (Fig. 2*F*). We found a hierarchy in the disruptive impact of different types of heterogeneities, with synaptic heterogeneity producing the largest reduction to grid score, followed by afferent heterogeneity. Intrinsic heterogeneity was the least disruptive in the emergence of grid-cell activity, whereby a high degree of heterogeneity was required to hamper grid pattern formation (Fig. 2*E–F*). Simultaneous progressive introduction of all three forms of heterogeneities at multiple degrees resulted in a similar progression of grid-pattern disruption (Fig. 2*E–F*). The introduction of the highest degree of all heterogeneities into the CAN model resulted in a complete loss of patterned activity and a marked reduction in the grid score values of all neurons in the network (Fig. 2*E–F*). We confirmed that these results were not artifacts of specific network initialization choices by observing similar grid score reductions in five additional trials with distinct initializations of CAN networks endowed with all three forms of heterogeneities (Fig. S2*F*). In addition, to rule out the possibility that these conclusions were specific to the choice of the virtual trajectory employed, we repeated our simulations and analyses with a different virtual trajectory (Fig. S3*A*) and found similar reductions in grid score with increase in the degree of all heterogeneities (Fig. S3*B*).

Furthermore, detailed quantitative analysis of grid cell activity showed that the introduction of heterogeneities did not result in marked population-wide changes to broad measures such as average firing rate, mean size of grid fields and average grid spacing (Fig. 3, Figs. S2–S3). Instead, the introduction of parametric heterogeneities resulted in a loss of spatial selectivity and disruption of patterned activity, reflected as progressive reductions in grid score, peak firing rate, information rate and sparsity (Figs. 2–3, Figs. S2–S3). We plotted pair-wise graphs of grid score values *vs.* τ or α or the jitter in W_{ij} (computed as a root-mean square error from W_{ij} in the homogeneous network) for each neuron in networks endowed with different degrees of the associated heterogeneity. Our results showed that in networks with intrinsic or afferent heterogeneities, grid score of individual neurons was not dependent on the actual value of the associated parameter (τ or α, respectively), but was critically reliant on the degree of heterogeneity (Fig. 3*H*). Specifically, for a given degree of intrinsic or afferent heterogeneity, the grid score value spanned similar ranges for the low or high value of the associated parameter; but grid score reduced with increased degree of heterogeneities.

In addition, grid score of cells reduced with increase in local synaptic jitter, which increased with the degree of synaptic heterogeneity (Fig. 3*H*).

Thus far, our analyses involved a CAN model with a specific size (60×60). Would our results on heterogeneity-driven disruption of grid-patterned activity extend to CAN models of other sizes? To address this, we repeated our simulations with networks of size 40×40, 50×50, 80×80 and 120×120, and introduced different degrees of all three forms of heterogeneities into the network. We found that the disruptive impact of heterogeneities on grid-patterned activity was consistent across all tested networks (Fig. S4*A*), manifesting as a reduction in grid score with increased degree of heterogeneities (Fig. S4*B*). Our results also showed that the disruptive impact of heterogeneities on grid-patterned activity increased with increase in network size. This size-dependence specifically manifested as a complete loss of spatially-selective firing patterns (Fig. S4*A*) and the consistent drop in the grid score value to zero (*i.e.,* %change = –100 in Fig. S4*B*) across all neurons in the 120×120 network with high degree of heterogeneities. We also observed a progressive reduction in the average and the peak-firing rates with increase in the degree of heterogeneities across all network sizes, although with a pronounced impact in networks with higher size (Fig. S5).

Together, our results demonstrated that the introduction of physiologically relevant heterogeneities into the CAN model resulted in a marked disruption of grid-patterned activity. The disruption manifested as a loss in spatial selectivity in the activity of individual cells in the network, progressively linked to the degree of heterogeneity. Although all forms of heterogeneities resulted in disruption of patterned activity, there was differential sensitivity to different heterogeneities, with heterogeneity in local network connectivity playing a dominant role in hampering spatial selectivity and patterned activity.

Incorporation of biological heterogeneities predominantly altered neural activity in low frequencies.

How does the presence of heterogeneities affect activity patterns of neurons in the network as they respond to the movement of the virtual animal? A systematic way to explore patterns of neural activity is to assess the relative power of specific frequency components in neural activity. Therefore, we subjected the temporal outputs of individual neurons (across the entire period of the simulation) to spectral analysis and found neural activity to follow a typical response curve that was dominated by lower frequency components, with little power in the higher frequencies (*e.g.,* Fig. 4*A,* HN). This is to be expected as a consequence of the low-pass filtering inherent to the neuronal model, reflective of membrane filtering.

How does the incorporation of these different forms of heterogeneities alter spectral characteristics of neuronal temporal activity patterns? To address this, we performed spectral analyses of temporal activity patterns of neurons from networks endowed with different forms of heterogeneities at various degrees (Fig. 4). As biological heterogeneities were incorporated by reducing or increasing default parameter values (Table S1), there was considerable variability in how individual neurons responded to such heterogeneities (Fig. 4). Specifically, when compared against the respective neuron in the homogeneous network, some neurons showed increases in activity magnitude at certain frequencies and others showed a reduction in magnitude (*e.g.*, Fig. 4*A*). To quantify this variability in neuronal responses, we first computed the difference between frequency-dependent activity profiles of individual neurons obtained in the presence of specific heterogeneities and of the same neuron in the homogeneous network (with identical initial conditions, and subjected to identical afferent inputs). We computed activity differences for all the 3600 neurons in the network, and plotted the variance of these differences as a function of frequency (*e.g.,* Fig. 4*B*). Strikingly, we found that the impact of introducing biological heterogeneities predominantly altered lower frequency components of neural activity, with little to no impact on higher frequencies. In addition, the variance in the deviation of neural activity from the homogenous network progressively increased with higher degrees of heterogeneities, with large deviations occurring in the lower frequencies (Fig. 4).

Together, these observations provided an important insight that the presence of physiologically relevant network heterogeneities predominantly affected lower frequency components of neural activity, with higher degrees of heterogeneity yielding larger variance in the deviation of low-frequency activity from the homogeneous network.

Introducing intrinsic resonance in rate-based neurons.

Several cortical and hippocampal neuronal structures exhibit intrinsic resonance, which allows these structures to maximally respond to a specific input frequency, with neural response falling on either side of this resonance frequency (49, 50, 62-65). More specifically, excitatory (66-76) and inhibitory neurons (77) in the superficial layers of the medial entorhinal cortex manifest resonance in the theta frequency range (4–10 Hz). Therefore, the model of individual neurons in the CAN model as integrators of afferent activity is inconsistent with the resonating structure intrinsic to their physiological counterparts. Intrinsic resonance in neurons is mediated by the expression of slow restorative ion channels, such as the HCN or the *M*-type potassium, which suppress low-frequency inputs by virtue of

their kinetics and voltage-dependent properties (49, 50). As the incorporation of biological heterogeneities predominantly altered low-frequency neural activity (Fig. 4), we hypothesized that the expression of intrinsic neuronal resonance (especially the associated suppression of low-frequency components) could counteract the disruptive impact of biological heterogeneities on network activity, thereby stabilizing grid-like activity patterns.

An essential requirement in testing this hypothesis was to introduce intrinsic resonance in the rate-based neuronal models in our network. To do this, we noted that the integrative properties of the integrator model neuron are mediated by the low-pass filtering kinetics associated with the parameter τ. We confirmed the low-pass filter (LPF) characteristics of the integrator neurons by recording the response of individual neurons to a chirp stimulus (Fig. 5*A–B*). As this provides an equivalent to the LPF associated with the membrane time constant, we needed a high-pass filter (HPF) to mimic the mechanistic route of neuronal structures in introducing resonance into our model. A simple approach to suppress low-frequency components is to introduce a differentiator, which we confirmed by passing a chirp stimulus through a differentiator (Fig. 5*A*, Fig. 5*C*). We therefore passed the outcome of the integrator (endowed with LPF characteristics) through a first-order differentiator (HPF), with the postulate that the net transfer function would manifest resonance. We tested this by first subjecting a chirp stimulus to the integrator neuron dynamics, and feeding that output to the differentiator. We found that the net output expressed resonance, acting as a band-pass filter (Fig. 5*A*, Fig. 5*C*).

Physiologically, tuning of intrinsic resonance to specific frequencies could be achieved by altering the characteristics of the high- or the low-pass filters (29, 49, 50, 65, 78-82). Mechanistically matching this physiological tuning procedure, we tuned resonance frequency (f_R) in our rate-based resonator model by either changing τ that governs the LPF (Figs. 5*D–E*) or by altering an exponent ε (equation 9) that regulated the slope of the HPF on the frequency axis (Fig. 5*F–G*). We found f_R to decrease with an increase in τ (Fig. 5*E*) or a reduction in ε (Fig. 5*G*). In summary, we mimicked the biophysical mechanisms governing resonance in neural structures to develop a phenomenological methodology to introduce and tune intrinsic resonance, yielding a tunable band-pass filtering structure, in rate-based model neurons.

Homogeneous CAN models constructed with resonator neurons exhibited stable grid-patterned neural activity.

How does the expression of intrinsic resonance in individual neurons of CAN models alter their grid-patterned neural activity? How do grid patterns respond to changes in resonance frequency, realized either by altering τ (Fig. 5*E*) or ε? To address these, we replaced all neurons in the homogeneous CAN model with resonators, and presented the network with the same virtual trajectory (Fig. 2*E*). We found that CAN models with resonators were able to reliably and robustly produce grid-patterned neural activity, which were qualitatively (Fig. 6*A–B*) and quantitatively (Fig. 6*C–F*, Fig. S6) similar to patterns produced by networks of integrator neurons across different values of τ. Importantly, increase in τ markedly increased spacing between grid fields (Fig. 6*D*) and their average size (Fig. 6*E*), consequently reducing the number of grid fields within the arena (Fig. 6*F*). It should be noted that the reduction in grid score with increased τ (Fig. 6*C*) is merely a reflection of the reduction in the number of grid patterns within the arena, and not indicative of loss of grid-patterned activity. Although the average firing rates were tuned to be similar across the resonator and the integrator networks (Fig. S6*A*), the peak-firing rate in the resonator network was significantly higher (Fig. S6*B*). In addition, for both resonator and integrator networks, consistent with increases in grid-field size and spacing, there were marked increases in information rate (Fig. S6*C*) and reductions in sparsity (Fig. S6*D*) with increase in τ.

Within our model framework, it is important to emphasize that although increasing τ reduced f_R in resonator neurons (Fig. 5*E*, Fig. 6*B*), the changes in grid spacing and size are not a result of change in f_R, but a consequence of altered τ. This inference follows from the observation that altering τ has qualitatively and quantitatively similar outcomes on grid spacing and size in both integrator and resonator networks (Fig. 6). Further confirmation for the absence of a direct role for f_R in regulating grid spacing or size (within our modeling framework) came from the invariance of grid spacing and size to change in ε, which altered f_R (Fig. 7). Specifically, when we fixed τ, and altered ε across resonator neurons in the homogeneous CAN model, f_R of individual neurons changed (Fig. 7*A*), but did not markedly change grid field patterns (Fig. 7*A*), grid score, average grid spacing, mean size, number or sparsity of grid fields (Fig. 7*B*). However, increasing ε decreased grid-field sizes, the average and the peak firing rates, consequently reducing the information rate in the activity pattern (Fig. 7*B*).

Together, these results demonstrated that homogeneous CAN models with resonators reliably and robustly produce grid-patterned neural activity. In these models, the LPF regulated the size and spacing of the grid fields and the HPF governed the magnitude of activity and the suppression of low-frequency inputs.

Resonating neurons stabilized the emergence of grid-patterned activity in heterogeneous CAN models.

Having incorporated intrinsic resonance into the CAN model, we were now equipped to directly test our hypothesis that the expression of intrinsic neuronal resonance could stabilize grid-like activity patterns in heterogeneous networks. To do this, we incorporated heterogeneities, retaining the same forms/degrees of heterogeneities (Table S1; Fig. 2*A–D*) and the same virtual trajectory (Fig. 2*E*), in a CAN model endowed with resonators rather than integrators. We simultaneously introduced all three forms of heterogeneities at 5 different degrees into the CAN model with resonator neurons, and obtained the spatial activity maps for individual neurons (Fig. 8*A*). Qualitatively, we observed that the presence of resonating neurons in the CAN model stabilized grid-patterned activity in individual neurons, despite the introduction of the highest degrees of all forms of biological heterogeneities (Fig. 8*A*). Importantly, outputs produced by the homogeneous CAN model manifested spatially precise circular grid fields, exhibiting regular triangular firing patterns across trials (*e.g.*, Fig. 1*A*), which constituted forms of precision that are not observed in electrophysiologically obtained grid-field patterns (60, 61). However, that with the incorporation of biological heterogeneities in resonator neuron networks, the imprecise shapes and stable patterns of grid-patterned firing (*e.g.*, Fig. 8*A*) tend closer to those of biologically observed grid cells. Quantitatively, we computed grid-cell measurements across all the 3600 neurons in the network, and found that all quantitative measurements (Fig. 8*B–I*, Fig. S7), including the grid score (Fig. 8*B*) and information rate (Fig. 8*H*), were remarkably robust to the introduction of heterogeneities (*cf.* Fig. 2 and Fig. S2 for CAN models with integrator neurons).

To ensure that the robust emergence of stable grid-patterned activity in heterogeneous CAN networks with resonator neurons was not an artifact of the specific network under consideration, we repeated our analyses with two additional sets of integrator-resonator comparisons (Fig. S8). In these networks, we employed a baseline τ of either 14 ms (Fig. S8*A*) or 8 ms (Fig. S8*B*) instead of the 10 ms value employed in the default network (Fig. 2, Fig. 8). A pairwise comparison of all grid-cell measurements between networks with

integrator *vs.* resonator neurons demonstrated that the resonator networks were resilient to the introduction of heterogeneities compared to integrator networks (Fig. S8).

The grid-cell activity on a 2D plane represents a spatially repetitive periodic pattern. Consequently, a phase plane constructed from activity along the diagonal of the 2D plane on one axis (Fig. S9*A*), and the spatial derivative of this activity on the other should provide a visual representation of the impact of heterogeneities and resonance on this periodic pattern of activity. To visualize the specific changes in the periodic orbits obtained with homogeneous and heterogeneous networks constructed with integrators or resonators, we plotted the diagonal activity profiles of 5 randomly picked neurons using the phase plane representation (Fig. S9*B*). This visual representation confirmed that homogenous CAN models built of integrators or resonators yielded stable closed orbit trajectories, representing similarly robust grid-patterned periodic activity (Fig. S9*B*). The disparate sizes of different orbits are merely a reflection of the intersection of the diagonal with a given grid-field. Specifically, if the grid fields were considered to be ideal circles, the orbital size is the largest if diagonal passes through the diameter, with orbital size reducing for any other chord.

Upon introduction of heterogeneities, the phase-plane plots of diagonal activity profiles from the heterogeneous integrator network lacked closed orbits (Fig S9*B*). This is consistent with drastic decrease in grid score and information rate reported for these heterogeneous network models (Figs. 2–3). In striking contrast, the phase-plane plots from the heterogeneous resonator network manifested closed orbits even with the highest degree of heterogeneities introduced (Fig. S9*B*). Although these phase-plane trajectories were noisy compared to those from the homogeneous resonator network, the presence of closed orbits indicated the manifestation of spatial periodicity in these activity patterns (Fig. S9*B*). These observations visually demonstrated that resonator neurons stabilized the heterogeneous network, and maintained spatial periodicity in grid-cell activity.

Together, these results demonstrated that incorporating intrinsic resonance into neurons of the CAN model imparts resilience to the network, facilitating the robust emergence of stable grid-cell activity patterns, despite the expression of biological heterogeneities in neuronal and synaptic properties.

Resonating neurons suppressed the impact of biological heterogeneities on low-frequency components of neural activity.

Our hypothesis on a potential role for intrinsic neuronal resonance in stabilizing grid-patterned firing in heterogeneous CAN models was centered on the ability of resonators in

suppressing low-frequency components. Although our analyses provided evidence for stabilization of grid-patterned firing, did resonance also suppress the impact of biological heterogeneities of low-frequency components of neural activity? To assess this, we performed frequency-dependent analyses of neural activity in CAN models with resonators (Fig. 9, Fig. S10–S11) and compared them with integrator-based CAN models (Fig. 4). First, we found that the variance in the deviations of neural activity in heterogeneous networks with reference to the respective homogeneous models were considerably lower with resonator neurons, compared to integrator counterparts (Fig. 9*A–B*, Fig. S11*A–B*). Second, comparing the relative power of neural activity across different octaves, we found that resonator networks suppressed lower frequencies (0–2 and 2–4 Hz octaves) and enhanced power in the range of neuronal resonance frequencies (4–10 Hz), when compared with their integrator counterparts (Fig. 9*C*, Fig. S11*C*). This relative suppression of low-frequency power accompanied by the relative enhancement of high-frequency power was observed across all resonator networks, either homogeneous (Fig. S10) or heterogeneous with distinct forms of heterogeneities (Fig. S11*C*).

Together, our results demonstrated that biological heterogeneities predominantly altered low-frequency components of neural activity, and provide strong quantitative lines of evidence that intrinsic neuronal resonance play a stabilizing role in heterogeneous networks by suppressing low-frequency inputs, thereby counteracting the disruptive impact of biological heterogeneities on low-frequency components.

DISCUSSION

The principal conclusion of this study is that intrinsic neuronal resonance stabilizes heterogeneous 2D CAN models, by suppressing heterogeneity-induced perturbations in low-frequency components of neural activity.

A physiological role for intrinsic neuronal resonance in stabilizing heterogeneous neural networks.

Intrinsic neuronal resonance is effectuated by the expression of resonating conductances, which are mediated by restorative channels endowed with activation time constants slower than the neuronal membrane time constant (49). The gating properties and the kinetics of these ion channels allow them to suppress low-frequency activity with little to no impact on higher frequencies, yielding resonance in conjunction with the low-pass filter governed by the membrane time constant (49). This intrinsic form of neuronal resonance, mediated by ion channels that are intrinsic to the neural structure, is dependent on membrane voltage (50, 64, 83), somato-dendritic recording location (50, 64, 83), neuronal location along the dorso-ventral axis (68, 73, 76, 84, 85) and is regulated by neuromodulators (86, 87), activity-dependent plasticity (64, 88-90) and pathological conditions (91-93). Resonating conductances have been implicated in providing frequency selectivity to specific range of frequencies under sub- and supra-threshold conditions (49, 62-65, 83, 94-96), in mediating membrane potential oscillations (81, 97, 98), in mediating coincidence detection through alteration to the class of neural excitability (65, 94-96, 99), in regulating spatio-temporal summation of synaptic inputs (73, 76, 100-104), in introducing phase leads in specific ranges of frequencies regulating temporal relationships of neural responses to oscillatory inputs (50, 105), in regulating local-field potentials and associated spike phases (106-108), in mediating activity homeostasis through regulation of neural excitability (64, 88, 89, 109-111), in altering synaptic plasticity profiles (74, 112, 113) and in regulating grid-cell scales (67, 68, 75, 114).

Our analyses provide an important additional role for intrinsic resonance in stabilizing heterogeneous neural network, through the suppression of heterogeneity-induced perturbation in low-frequency components. The $1/f$ characteristics associated with neural activity implies that the power in lower frequencies is higher (58), and our analyses show that the incorporation of biological heterogeneities into networks disrupt their functional outcomes by introducing perturbations predominantly in the lower frequencies. We demonstrate that resonating conductances, through their ability to suppress low-frequency activity, are ideally

placed to suppress such low-frequency perturbations thereby stabilizing activity patterns in the face of biological heterogeneities. As biological heterogeneities are ubiquitous, we postulate intrinsic neuronal resonance as a powerful mechanism that lends stability across different heterogeneous networks, through suppression of low-frequency perturbations introduced by the heterogeneities. A corollary to this postulate is that the specific resonance frequency of a given neural structure is a reflection of the need to suppress frequencies where the perturbations are introduced by specific forms and degree of biological heterogeneities expressed in the network where the structure resides.

Within this framework, the dorso-ventral gradient in resonance frequencies in entorhinal stellate cells could be a reflection of the impact of specific forms of heterogeneities expressed along the dorso-ventral axis on specific frequency ranges, with resonance frequency being higher in regions where a larger suppression of low-frequency components is essential. Future electrophysiological and computational studies could specifically test this hypothesis by quantifying the different heterogeneities in these sub-regions, assessing their frequency-dependent impact on neural activity in individual neurons and their networks. More broadly, future studies could directly measure the impact of perturbing resonating conductances on network stability and low-frequency activity in different brain regions to test our predictions on the relationship among biological heterogeneities, intrinsic resonance and network stability.

Future directions and considerations in model interpretation.

Our analyses here employed a rate-based CAN model for the generation of grid-patterned activity. Rate-based models are inherently limited in their ability to assess temporal relationships between spike timings, which are important from the temporal coding perspective where spike timings with reference to extracellular oscillations have been shown to carry spatial information within grid fields (115). Additionally, the CAN model is one of the several theoretical and computational frameworks that have been proposed for the emergence of grid cell activity patterns, and there are lines of experimental evidence that support aspects of these distinct models (30-32, 34, 36, 116-127). Within some of these frameworks, resonating conductances have been postulated to play specific roles, distinct from the one proposed in our study, in the emergence of grid-patterned activity and the regulation of their properties (67, 68, 75, 114, 121). Together, the use of the rate-based CAN model has limitations in terms of assessing temporal relationships between oscillations and spike timings, and in deciphering the other potential roles of resonating conductances in grid-

patterned firing. However, models that employ other theoretical frameworks do not explicitly incorporate the several heterogeneities in afferent, intrinsic and synaptic properties of biological networks, including those in the conductance and gating properties of resonating conductances. Future studies should therefore explore the role of resonating conductances in stabilizing conductance-based grid-cell networks that are endowed with all forms of biological heterogeneities. Such conductance-based analyses should also systematically assess the impact of resonating conductances, their kinetics and gating properties (including associated heterogeneities) in regulating temporal relationships of spike timings with theta-frequency oscillations spanning the different theoretical frameworks.

A further direction for future studies could be the use of morphologically realistic conductance-based model neurons, which would enable the incorporation of the distinct ion-channels and receptors distributed across the somato-dendritic arborization. Such models could assess the role of interactions among several somato-dendritic conductances, especially with resonating conductances, in regulating grid-patterned activity generation (121, 127). In addition, computations performed by such a morphologically realistic conductance-based neuron are more complex than the simplification of neural computation as an integrator or a resonator (117, 128-130). For instance, owing to differential distribution of ionic conductances, different parts of the neurons could exhibit integrator- or resonator-like characteristics, with interactions among different compartments yielding the final outcome (65, 94-96, 131). The conclusions of our study emphasizing the importance of biological heterogeneities and resonating conductances in grid-cell models underline the need for heterogeneous morphologically realistic conductance-based network models to systematically compare different theoretical frameworks for grid-cell emergence. Future studies should endeavor to build such complex heterogeneous networks, endowed with synaptic and channel noise, in systematically assessing the role of heterogeneities and specific ion-channel conductances in the emergence of grid-patterned neural activity across different theoretical frameworks.

In summary, our analyses demonstrated that incorporation of different forms of biological heterogeneities disrupted network functions through perturbations that were predominantly in the lower frequency components. We showed that intrinsic neuronal resonance, a mechanism that suppressed low-frequency activity, stabilized network function. As biological heterogeneities are ubiquitous and as the dominance of low-frequency perturbations is pervasive across biological networks (55-59), we postulate that mechanisms that suppress low-frequency components could be a generalized route to stabilize heterogeneous biological networks.

METHODS

Development of a virtual trajectory to reduce computational cost.

We developed the following algorithm to yield faster virtual trajectories in either a circular (2 m diameter) or a square (2 m × 2 m) arena:

1. The starting location of the virtual animal was set at the center of the arena (x_0=1, y_0=1).
2. At each time step (=1 ms), two random numbers were picked, one denoting distance from a uniform distribution ($d_t \in [0, 0.004]$) and another yielding the angle of movement from another uniform distribution ($A_t \in [-\pi/36,\ \pi/36]$). The angle of movement was restricted to within $\pi/36$ on either side to yield smooth movements within the spatial arena. The new coordinate of the animal was then updated as:

$$x_t = x_{t-1} + d_t\ \sin(A_t) \tag{1}$$

$$y_t = y_{t-1} + d_t \cos(A_t) \tag{2}$$

   If the new location (x_t, y_t) fell outside the arena, the d_t and A_t are repicked until (x_t, y_t) were inside the bounds of the arena.
3. To enable sharp turns near the boundaries of the arena, the A_t random variable was picked from a uniform distribution of ($A_t \in [0, 2\pi]$) instead of uniform distribution of ($A_t \in [-\pi/36, \pi/36]$) if either x_{t-1} or y_{t-1} was close to arena boundaries. This enhanced range for A_t closed to the boundaries ensured that there was enough deflection in the trajectory to mimic sharp turns in animal runs in open arena boundaries.

The limited range of $A_t \in [-\pi/36,\ \pi/36]$ in step 2 ensured that the head direction and velocity inputs to the neurons in the CAN network were not changing drastically at every time step of the simulation run, thereby stabilizing spatial activity. We found the virtual trajectories yielded by this algorithm to closely mimic animal runs in an open arena, with better control over simulation periods and better computational efficiency in terms of covering the entire arena within shorter time duration.

Structure and dynamics of the continuous attractor network model with integrator neurons.

Each neuron in the network has a preferred direction θ_i (assumed to receive input from specific head direction cells), which can take its value to be among 0, π/2, π and 3π/2 respectively depicting east, north, west and south. The network was divided into local blocks of four cells representing each of these four directions and local blocks were uniformly tiled to span the entire network. This organization translated to a scenario where one-fourth of the

neurons in the network were endowed with inputs that had the same direction preference. Of the two sets of synaptic inputs to neurons in the network, intra-network inputs followed a Mexican-hat connectivity pattern. The recurrent weights matrix for Mexican-hat connectivity was achieved through the difference of Gaussian equation, given by (30):

$$W_{ij} = W_0(\boldsymbol{x}_i - \boldsymbol{x}_j - l\hat{e}_{\theta j}) \tag{3}$$

$$W_0(\boldsymbol{x}) = a\exp(-\gamma|\boldsymbol{x}|^2) - \exp(-\beta|\boldsymbol{x}|^2) \tag{4}$$

where W_{ij} represented the synaptic weight from neuron j (located at $\boldsymbol{x}_j$) to neuron i (located at $\boldsymbol{x}_i$), $\hat{e}_{\theta j}$ defined the unit vector pointing along the θ_j direction. This weight matrix was endowed with a center-shifted center-surround connectivity, and the parameter l (default value: 2) defined the amount of shift along $\hat{e}_{\theta j}$. In the difference of Gaussians formulation in equation 6, the parameter a regulated the sign of the synaptic weights and was set to 1, defining an all-inhibitory network. The other parameters were $\gamma = 1.1\times\beta$ with $\beta = 3/\lambda^2$, and λ (default value: 13) defining the periodicity of the lattice (30).

The second set of synaptic inputs to individual neurons, arriving as feed-forward inputs based on the velocity of the animal and the preferred direction of the neuron, was computed as:

$$B_i = 1 + \alpha\hat{e}_{\theta j} \cdot \boldsymbol{v} \tag{5}$$

where α denotes a gain parameter for the velocity inputs (velocity scaling factor), $\boldsymbol{v}$ represents the velocity vector derived from the trajectory of the virtual animal.

The dynamics of the rate-based integrator neurons, driven by these two sets of inputs was then computed as:

$$\tau\frac{dS_i}{dt} + S_i = f\left(\sum_j W_{ij}S_j + B_i\right) \tag{6}$$

where f represented the neural transfer function, which was implemented as a simple rectification non-linearity, and $S_i(t)$ denoted the activity of neuron i at time point t. The default value of the integration time constant (τ) of neural response was 10 ms. CAN models were initialized with randomized values of S_i ($S_i^0 \in [0,1]$) for all neurons. For stable spontaneous pattern to emerge over the neural lattice, an initial constant feed-forward drive was provided by ensuring the velocity input was zero for the initial 100-ms period. The time step (dt) for numerical integration was 0.5 ms when we employed the real trajectory and 1 ms for simulations with virtual trajectories. We confirmed that the use of 1-ms time steps for virtual trajectories did not hamper accuracy of the outcomes. Activity patterns of all neurons

were recorded for each time step. For visualization of the results, the spike threshold was set at 0.1 (a.u.).

Incorporating biological heterogeneities into the CAN model.

We introduced intrinsic, afferent and synaptic forms of biological heterogeneities by independently randomizing the values of integration time constant (τ), velocity scaling factor (α) and the connectivity matrix (W_{ij}), respectively, across neurons in the CAN model. Specifically, in the homogeneous CAN model, these parameters were set to a default value and were identical across all neurons in the network. However, in heterogeneous networks, each neuron in the network was assigned a different value for these parameters, each picked from respective uniform distributions (Table1). We progressively expanded the ranges of the respective uniform distributions to progressively increase the degree of heterogeneity (Table S1). We built CAN models with four different forms of heterogeneities: networks that were endowed with one of intrinsic, afferent and synaptic forms of heterogeneities, and networks that expressed all forms together. In networks that expressed only one form of heterogeneity, the other two parameters were set identical across all neurons. In networks expressing all forms of heterogeneities, all three parameters were randomized with the span of the uniform distribution for each parameter concurrently increasing with the degree of heterogeneity (Table S1). We simulated different trials of a CAN model by employing different sets of initial randomization of activity values (S_i^0) for all the cells, while keeping all other model parameters (including the connectivity matrix, trajectory and the specific instance of heterogeneities) unchanged (Fig. S2).

Introducing resonance in rate-based neurons.

To assess the frequency-dependent response properties, we employed a chirp stimulus $c_{100}(t)$, defined a constant-amplitude sinusoidal input with its frequency linearly increasing as a function of time, spanning 0–100 Hz in 100 s. We fed $c_{100}(t)$ as the input to a rate-based model neuron and recorded the response of the neuron:

$$\tau \frac{ds}{dt} + s = c_{100} \tag{7}$$

We computed the Fourier transform of the response $s(t)$ as $S(f)$ and employed the magnitude of $S(f)$ to evaluate the frequency-dependent response properties of the neuron. Expectedly, the integrator neuron acted as a low-pass filter (Fig. 5*A–B*).

A simple means to elicit resonance from the response of a low-pass system is to feed the output of the low-pass system to a high pass filter (HPF), and the interaction between these filters results in resonance (49, 50). We tested this employing the $c_{100}(t)$ stimulus, by using the low-pass response $s(t)$ to the chirp stimulus from equation 7:

$$h = s\left(\frac{ds}{dt}\right)^{\varepsilon} \tag{8}$$

Here, $h(t)$ represented the output of the resultant resonator neuron, ε defined an exponent that regulates the slope of the frequency-selective response properties of the high pass filter. When $\varepsilon = 0$, $h(t)$ trivially falls back to the low-pass response $s(t)$. The magnitude of the Fourier transform of $h(t)$, $H(f)$ manifested resonance in response to the $c_{100}(t)$ stimulus (Fig. 5*A*, Fig. 5*C*).

Having confirmed that the incorporation of a high-pass filter would yield resonating dynamics, we employed this formulation to define the dynamics of a resonator neuron in the CAN model through the combination of the existing low-pass kinetics (equation 6) and the high-pass kinetics. Specifically, we obtained S_i for each neuron i in the CAN model from equation 6, and redefined neural activity as the product of this S_i (from equation 6) and its derivative raised to an exponent:

$$S_i := RS_i\left(\frac{dS_i}{dt}\right)^{\varepsilon} \tag{9}$$

where, R was a scaling factor for matching the response of resonator neurons with integrator neurons and ε defined the exponent of the high pass filter. Together, whereas the frequency-dependent response of the integrator is controlled by integration time constant (τ), that of a resonator is dependent on τ of the integrator as well as the HPF exponent ε (Figs. 5*D*–*E*).

To simulate homogeneous CAN models with resonator neurons, all integrator neurons in the standard homogeneous model (equations 3–6) were replaced with resonator neurons. Intrinsic, synaptic and afferent heterogeneities are introduced as previously described (Table S1) to build heterogeneous CAN models with resonator neurons. The other processes, including initialization procedure of the resonator neuron network were identical to the integrator neuron network. In simulations where τ was changed from its base value of 10 ms, the span of uniform distributions that defined the five degrees of heterogeneities were appropriately rescaled and centered at the new value of τ. For instance, when τ was set to 8 ms, the spans of the uniform distribution for the first and the fifth degrees of heterogeneity were 6.4–9.6 ms (20% of the base value on either side), and 1–16 ms (100% of the base value on either side, with an absolute cutoff at 1 ms), respectively.

Quantitative analysis of grid cell activity.

To quantitative assess the impact of heterogeneities and the introduction of resonance into the CAN neurons, we employed standard measurements of grid-cell activity (60, 61).

We divided the space of the open arena into 100×100 pixels to compute the rate maps of grid cell activity in the network. Activity spatial maps were constructed for each cell by taking the activity (S_i for cell i) of the cell at each time stamp and synchronizing the index of corresponding (x, y) location of the virtual animal in the open arena, for the entire duration of the simulation. Occupancy spatial maps were constructed by computing the probability (p_m) of finding the rat in m^{th} pixel, employing the relative time spent by the animal in that pixel across the total simulation period. Spatial rate maps for each cell in the network were computed by normalizing their activity spatial maps by the occupancy spatial map for that run. Spatial rate maps were smoothened using a 2D-Gaussian kernel with standard deviation (σ) of 2 pixels (*e.g.*, Fig. 1*A*, panels in the bottom row for each value of T_{run}). *Average firing rate* (μ) of grid cells was computed by summing the activity of all the pixels from rate map matrix and dividing this quantity by the total number of pixels in the rate map (N =10,000). *Peak firing rate* ($\mu_{\max}$) of a neuron was defined as the highest activity value observed across all pixels of its spatial rate map.

For estimation of grid fields, we first detected all local maxima in the 2D-smoothened version of the spatial rate maps of all neurons in the CAN model. Individual grid-firing fields were identified as contiguous regions around the local maxima, spatially spreading to a minimum of 20% activity relative to the activity at the location of the local maxima. The *number of grid fields* corresponding to each grid cell was calculated as the total number of local peaks detected in the spatial rate map of the cell. The *mean size of the grid fields* for a specific cell was estimated by calculating the ratio between the total number of pixels covered by all grid fields and the number of grid fields. The *average grid-field spacing* for individual grid cells was computed as the ratio of the sum of distances between the local peaks of all grid fields in the rate map to the total number of distance values.

Grid score was computed by assessing rotational symmetry in the spatial rate map. Specifically, for each neuron in the CAN model, the spatial autocorrelation value, SAC_{φ}, was computed between its spatial rate map and the map rotated by $\varphi°$, for different values of φ (30, 60, 90, 120 or 150). These SAC_{φ} values were used for calculating the grid score for the given cell as:

$$\text{Grid score} = \min(SAC_{60},\ SAC_{120}) - \max(SAC_{30},\ SAC_{90}, SAC_{150}) \tag{10}$$

Spatial information rate (I_S) in bits per sec was calculated by:

$$I_S = \sum_m p_m \, \mu_m \log_2 \frac{\mu_m}{\mu} \tag{11}$$

where p_m defined the probability of finding the rat in m^{th} pixel, μ_m represented the mean firing rate of the grid cell in the mth pixel and μ denoted the average firing rate of grid cell. *Sparsity* was computed as the ratio between the square mean rate and mean square rate:

$$\text{Sparsity} = \frac{\mu^2}{\sum_i p_i \, \mu_i^2} \tag{12}$$

Quantitative analysis of grid cell temporal activity in the spectral domain.

To understand the impact of network heterogeneities on spectral properties of grid cell activities under the CAN framework, we used the Fourier transform of the temporal activity of all the grid cells in a network. First, we assessed the difference in the magnitude spectra of temporal activity of the grid cells (n = 3600) in the homogeneous network compared to the corresponding grid cells in the heterogeneous networks (*e.g.,* Fig. 4*A*). Next, we normalized this difference in magnitude spectra for each grid cell with respect to the sum of their respective maximum magnitude for the homogeneous and the heterogeneous networks. Finally, we computed the variance of this normalized difference across all the cells in the networks (*e.g.,* Fig. 4*B*).

Furthermore, to perform octave analysis on the magnitude spectra of the temporal activity of the grid cells, we computed the percentage of area under the curve (AUC) for each octave (0–2 Hz, 2–4 Hz, 4–8 Hz, 8–16 Hz) from the magnitude spectra (Fig. S10*B*-*C*). We performed a similar octave analysis on the variance of normalized difference for networks endowed with integrator or resonator neurons (Fig. 9*B*, Fig. S11*D*–*F*).

Computational details.

Grid cell network simulations were performed in MATLAB 2018a (Mathworks Inc., USA) with a simulation step size of 1 ms, unless otherwise specified. All data analyses and plotting were performed using custom-written software within the IGOR Pro (Wavemetrics, USA) or MATLAB environments, and all statistical analyses were performed using the R statistical package (132). To avoid false interpretations and to emphasize heterogeneities in simulation outcomes, the entire range of measurements are reported in figures rather than providing only the summary statistics (18, 29).

REFERENCES

1. Barkai N & Shilo BZ (2007) Variability and robustness in biomolecular systems. *Molecular cell* 28(5):755-760.
2. Maslov S & Sneppen K (2002) Specificity and stability in topology of protein networks. *Science* 296(5569):910-913.
3. Félix MA & Barkoulas M (2015) Pervasive robustness in biological systems. *Nature reviews. Genetics* 16(8):483-496.
4. Kitano H (2007) Towards a theory of biological robustness. *Molecular systems biology* 3:137.
5. Stelling J, Sauer U, Szallasi Z, Doyle FJ, 3rd, & Doyle J (2004) Robustness of cellular functions. *Cell* 118(6):675-685.
6. Turrigiano GG & Nelson SB (2000) Hebb and homeostasis in neuronal plasticity. *Current opinion in neurobiology* 10(3):358-364.
7. Turrigiano G (2011) Too many cooks? Intrinsic and synaptic homeostatic mechanisms in cortical circuit refinement. *Annu Rev Neurosci* 34:89-103.
8. Marder E & Goaillard JM (2006) Variability, compensation and homeostasis in neuron and network function. *Nature reviews. Neuroscience* 7(7):563-574.
9. Marder E (2011) Variability, compensation, and modulation in neurons and circuits. *Proc Natl Acad Sci U S A* 108 Suppl 3:15542-15548.
10. Marder E, Goeritz ML, & Otopalik AG (2015) Robust circuit rhythms in small circuits arise from variable circuit components and mechanisms. *Current opinion in neurobiology* 31:156-163.
11. Edelman GM & Gally JA (2001) Degeneracy and complexity in biological systems. *Proc Natl Acad Sci U S A* 98(24):13763-13768.
12. Prinz AA, Bucher D, & Marder E (2004) Similar network activity from disparate circuit parameters. *Nat Neurosci* 7(12):1345-1352.
13. Padmanabhan K & Urban NN (2010) Intrinsic biophysical diversity decorrelates neuronal firing while increasing information content. *Nat Neurosci* 13(10):1276-1282.
14. Voliotis M, Perrett RM, McWilliams C, McArdle CA, & Bowsher CG (2014) Information transfer by leaky, heterogeneous, protein kinase signaling systems. *Proceedings of the National Academy of Sciences of the United States of America* 111(3):E326-E333.
15. Shamir M & Sompolinsky H (2006) Implications of neuronal diversity on population coding. *Neural Comput* 18(8):1951-1986.
16. Chelaru MI & Dragoi V (2008) Efficient coding in heterogeneous neuronal populations. *Proc Natl Acad Sci U S A* 105(42):16344-16349.
17. Tripathy SJ, Padmanabhan K, Gerkin RC, & Urban NN (2013) Intermediate intrinsic diversity enhances neural population coding. *Proc Natl Acad Sci U S A* 110(20):8248-8253.
18. Marder E & Taylor AL (2011) Multiple models to capture the variability in biological neurons and networks. *Nat Neurosci* 14(2):133-138.
19. Gjorgjieva J, Drion G, & Marder E (2016) Computational implications of biophysical diversity and multiple timescales in neurons and synapses for circuit performance. *Current opinion in neurobiology* 37:44-52.
20. Goaillard JM, Taylor AL, Schulz DJ, & Marder E (2009) Functional consequences of animal-to-animal variation in circuit parameters. *Nat Neurosci* 12(11):1424-1430.

21. Grashow R, Brookings T, & Marder E (2010) Compensation for variable intrinsic neuronal excitability by circuit-synaptic interactions. *J Neurosci* 30(27):9145-9156.
22. Marder E, O'Leary T, & Shruti S (2014) Neuromodulation of circuits with variable parameters: single neurons and small circuits reveal principles of state-dependent and robust neuromodulation. *Annu Rev Neurosci* 37:329-346.
23. Angelo K, Rancz EA, Pimentel D, Hundahl C, Hannibal J, Fleischmann A, Pichler B, & Margrie TW (2012) A biophysical signature of network affiliation and sensory processing in mitral cells. *Nature* 488(7411):375-378.
24. Ecker AS, Berens P, Tolias AS, & Bethge M (2011) The effect of noise correlations in populations of diversely tuned neurons. *J Neurosci* 31(40):14272-14283.
25. Wang XJ & Buzsaki G (1996) Gamma oscillation by synaptic inhibition in a hippocampal interneuronal network model. *J Neurosci* 16(20):6402-6413.
26. Tikidji-Hamburyan RA, Martinez JJ, White JA, & Canavier CC (2015) Resonant Interneurons Can Increase Robustness of Gamma Oscillations. *J Neurosci* 35(47):15682-15695.
27. Renart A, Song P, & Wang XJ (2003) Robust spatial working memory through homeostatic synaptic scaling in heterogeneous cortical networks. *Neuron* 38(3):473-485.
28. Mishra P & Narayanan R (2019) Disparate forms of heterogeneities and interactions among them drive channel decorrelation in the dentate gyrus: Degeneracy and dominance. *Hippocampus* 29(4):378-403.
29. Rathour RK & Narayanan R (2019) Degeneracy in hippocampal physiology and plasticity. *Hippocampus* 29(10):980-1022.
30. Burak Y & Fiete IR (2009) Accurate path integration in continuous attractor network models of grid cells. *PLoS computational biology* 5(2):e1000291.
31. Couey JJ, Witoelar A, Zhang SJ, Zheng K, Ye J, Dunn B, Czajkowski R, Moser MB, Moser EI, Roudi Y, & Witter MP (2013) Recurrent inhibitory circuitry as a mechanism for grid formation. *Nat Neurosci* 16(3):318-324.
32. Domnisoru C, Kinkhabwala AA, & Tank DW (2013) Membrane potential dynamics of grid cells. *Nature* 495(7440):199-204.
33. Knierim JJ & Zhang K (2012) Attractor dynamics of spatially correlated neural activity in the limbic system. *Annu Rev Neurosci* 35:267-285.
34. Schmidt-Hieber C & Hausser M (2013) Cellular mechanisms of spatial navigation in the medial entorhinal cortex. *Nat Neurosci* 16(3):325-331.
35. Yartsev MM, Witter MP, & Ulanovsky N (2011) Grid cells without theta oscillations in the entorhinal cortex of bats. *Nature* 479(7371):103-107.
36. Yoon K, Buice MA, Barry C, Hayman R, Burgess N, & Fiete IR (2013) Specific evidence of low-dimensional continuous attractor dynamics in grid cells. *Nat Neurosci* 16(8):1077-1084.
37. Knierim JJ & Neunuebel JP (2016) Tracking the flow of hippocampal computation: Pattern separation, pattern completion, and attractor dynamics. *Neurobiology of learning and memory* 129:38-49.
38. Tsodyks M (1999) Attractor neural network models of spatial maps in hippocampus. *Hippocampus* 9(4):481-489.
39. Wills TJ, Lever C, Cacucci F, Burgess N, & O'Keefe J (2005) Attractor dynamics in the hippocampal representation of the local environment. *Science* 308(5723):873-876.

40. Ben-Yishai R, Bar-Or RL, & Sompolinsky H (1995) Theory of orientation tuning in visual cortex. *Proc Natl Acad Sci U S A* 92(9):3844-3848.
41. Camperi M & Wang XJ (1998) A model of visuospatial working memory in prefrontal cortex: recurrent network and cellular bistability. *J Comput Neurosci* 5(4):383-405.
42. Compte A, Brunel N, Goldman-Rakic PS, & Wang XJ (2000) Synaptic mechanisms and network dynamics underlying spatial working memory in a cortical network model. *Cerebral cortex* 10(9):910-923.
43. Zhang K (1996) Representation of spatial orientation by the intrinsic dynamics of the head-direction cell ensemble: a theory. *J Neurosci* 16(6):2112-2126.
44. Samsonovich A & McNaughton BL (1997) Path integration and cognitive mapping in a continuous attractor neural network model. *J Neurosci* 17(15):5900-5920.
45. Seung HS, Lee DD, Reis BY, & Tank DW (2000) Stability of the memory of eye position in a recurrent network of conductance-based model neurons. *Neuron* 26(1):259-271.
46. Kim SS, Rouault H, Druckmann S, & Jayaraman V (2017) Ring attractor dynamics in the Drosophila central brain. *Science* 356(6340):849-853.
47. Stringer SM, Trappenberg TP, Rolls ET, & de Araujo IE (2002) Self-organizing continuous attractor networks and path integration: one-dimensional models of head direction cells. *Network* 13(2):217-242.
48. Moser EI, Moser MB, & McNaughton BL (2017) Spatial representation in the hippocampal formation: a history. *Nat Neurosci* 20(11):1448-1464.
49. Hutcheon B & Yarom Y (2000) Resonance, oscillation and the intrinsic frequency preferences of neurons. *Trends Neurosci* 23(5):216-222.
50. Narayanan R & Johnston D (2008) The h channel mediates location dependence and plasticity of intrinsic phase response in rat hippocampal neurons. *J Neurosci* 28(22):5846-5860.
51. Mauro A (1961) Anomalous impedance, a phenomenological property of time-variant resistance. An analytic review. *Biophysical journal* 1:353-372.
52. Mauro A, Conti F, Dodge F, & Schor R (1970) Subthreshold behavior and phenomenological impedance of the squid giant axon. *The Journal of general physiology* 55(4):497-523.
53. Cole KS & Baker RF (1941) Transverse Impedance of the Squid Giant Axon during Current Flow. *The Journal of general physiology* 24(4):535-549.
54. Cole KS (1968) *Membranes, ions and impulses: A chapter of classical biophysics* (University of California, Berkeley press, Berkeley).
55. Gisiger T (2001) Scale invariance in biology: coincidence or footprint of a universal mechanism? *Biological reviews of the Cambridge Philosophical Society* 76(2):161-209.
56. Gilden DL (2001) Cognitive emissions of 1/f noise. *Psychol Rev* 108(1):33-56.
57. Hausdorff JM & Peng C (1996) Multiscaled randomness: A possible source of 1/f noise in biology. *Physical review. E, Statistical physics, plasmas, fluids, and related interdisciplinary topics* 54(2):2154-2157.
58. Buzsaki G (2006) *Rhythms of the brain* (Oxford University Press, New York).
59. Ward LM (2001) *Dynamical Cognitive Science* (MIT Press, Cambridge, MA, USA).
60. Hafting T, Fyhn M, Molden S, Moser MB, & Moser EI (2005) Microstructure of a spatial map in the entorhinal cortex. *Nature* 436(7052):801-806.

61. Fyhn M, Molden S, Witter MP, Moser EI, & Moser MB (2004) Spatial representation in the entorhinal cortex. *Science* 305(5688):1258-1264.
62. Pike FG, Goddard RS, Suckling JM, Ganter P, Kasthuri N, & Paulsen O (2000) Distinct frequency preferences of different types of rat hippocampal neurones in response to oscillatory input currents. *J Physiol* 529 Pt 1:205-213.
63. Hu H, Vervaeke K, & Storm JF (2002) Two forms of electrical resonance at theta frequencies, generated by M-current, h-current and persistent Na+ current in rat hippocampal pyramidal cells. *J Physiol* 545(Pt 3):783-805.
64. Narayanan R & Johnston D (2007) Long-term potentiation in rat hippocampal neurons is accompanied by spatially widespread changes in intrinsic oscillatory dynamics and excitability. *Neuron* 56(6):1061-1075.
65. Das A, Rathour RK, & Narayanan R (2017) Strings on a Violin: Location Dependence of Frequency Tuning in Active Dendrites. *Front Cell Neurosci* 11:72.
66. Giocomo LM & Hasselmo ME (2008) Time constants of h current in layer ii stellate cells differ along the dorsal to ventral axis of medial entorhinal cortex. *J Neurosci* 28(38):9414-9425.
67. Giocomo LM & Hasselmo ME (2009) Knock-out of HCN1 subunit flattens dorsal-ventral frequency gradient of medial entorhinal neurons in adult mice. *J Neurosci* 29(23):7625-7630.
68. Giocomo LM, Zilli EA, Fransen E, & Hasselmo ME (2007) Temporal frequency of subthreshold oscillations scales with entorhinal grid cell field spacing. *Science* 315(5819):1719-1722.
69. Erchova I, Kreck G, Heinemann U, & Herz AV (2004) Dynamics of rat entorhinal cortex layer II and III cells: characteristics of membrane potential resonance at rest predict oscillation properties near threshold. *J Physiol* 560(Pt 1):89-110.
70. Haas JS & White JA (2002) Frequency selectivity of layer II stellate cells in the medial entorhinal cortex. *Journal of neurophysiology* 88(5):2422-2429.
71. Schreiber S, Erchova I, Heinemann U, & Herz AV (2004) Subthreshold resonance explains the frequency-dependent integration of periodic as well as random stimuli in the entorhinal cortex. *Journal of neurophysiology* 92(1):408-415.
72. Ferrante M, Shay CF, Tsuno Y, William Chapman G, & Hasselmo ME (2017) Post-Inhibitory Rebound Spikes in Rat Medial Entorhinal Layer II/III Principal Cells: In Vivo, In Vitro, and Computational Modeling Characterization. *Cerebral cortex* 27(3):2111-2125.
73. Garden DLF, Dodson PD, O'Donnell C, White MD, & Nolan MF (2008) Tuning of synaptic integration in the medial entorhinal cortex to the organization of grid cell firing fields. *Neuron* 60.
74. Nolan MF, Dudman JT, Dodson PD, & Santoro B (2007) HCN1 channels control resting and active integrative properties of stellate cells from layer II of the entorhinal cortex. *J Neurosci* 27(46):12440-12451.
75. Pastoll H, Ramsden HL, & Nolan MF (2012) Intrinsic electrophysiological properties of entorhinal cortex stellate cells and their contribution to grid cell firing fields. *Frontiers in neural circuits* 6:17.
76. Pastoll H, Garden DL, Papastathopoulos I, Sürmeli G, & Nolan MF (2020) Inter- and intra-animal variation in the integrative properties of stellate cells in the medial entorhinal cortex. *eLife* 9.
77. Boehlen A, Heinemann U, & Henneberger C (2016) Hierarchical spike clustering analysis for investigation of interneuron heterogeneity. *Neuroscience letters* 619:86-91.

78. Rathour RK, Malik R, & Narayanan R (2016) Transient potassium channels augment degeneracy in hippocampal active dendritic spectral tuning. *Scientific reports* 6:24678.
79. Rathour RK & Narayanan R (2012) Inactivating ion channels augment robustness of subthreshold intrinsic response dynamics to parametric variability in hippocampal model neurons. *J Physiol* 590(Pt 22):5629-5652.
80. Rathour RK & Narayanan R (2014) Homeostasis of functional maps in active dendrites emerges in the absence of individual channelostasis. *Proc Natl Acad Sci U S A* 111(17):E1787-1796.
81. Mittal D & Narayanan R (2018) Degeneracy in the robust expression of spectral selectivity, subthreshold oscillations and intrinsic excitability of entorhinal stellate cells. *Journal of neurophysiology* 120(2):576-600.
82. Zemankovics R, Kali S, Paulsen O, Freund TF, & Hajos N (2010) Differences in subthreshold resonance of hippocampal pyramidal cells and interneurons: the role of h-current and passive membrane characteristics. *J Physiol* 588(Pt 12):2109-2132.
83. Hu H, Vervaeke K, Graham LJ, & Storm JF (2009) Complementary theta resonance filtering by two spatially segregated mechanisms in CA1 hippocampal pyramidal neurons. *J Neurosci* 29(46):14472-14483.
84. Malik R, Dougherty KA, Parikh K, Byrne C, & Johnston D (2016) Mapping the electrophysiological and morphological properties of CA1 pyramidal neurons along the longitudinal hippocampal axis. *Hippocampus* 26(3):341-361.
85. Hönigsperger C, Marosi M, Murphy R, & Storm JF (2015) Dorsoventral differences in Kv7/M-current and its impact on resonance, temporal summation and excitability in rat hippocampal pyramidal cells. *J Physiol* 593(7):1551-1580.
86. Dembrow N & Johnston D (2014) Subcircuit-specific neuromodulation in the prefrontal cortex. *Frontiers in neural circuits* 8:54.
87. Dembrow NC, Chitwood RA, & Johnston D (2010) Projection-specific neuromodulation of medial prefrontal cortex neurons. *J Neurosci* 30(50):16922-16937.
88. Brager DH & Johnston D (2007) Plasticity of intrinsic excitability during long-term depression is mediated through mGluR-dependent changes in $I_{\rm h}$ in hippocampal CA1 pyramidal neurons. *J Neurosci* 27:13926-13937.
89. Narayanan R, Dougherty KJ, & Johnston D (2010) Calcium Store Depletion Induces Persistent Perisomatic Increases in the Functional Density of h Channels in Hippocampal Pyramidal Neurons. *Neuron* 68(5):921-935.
90. Malik R & Johnston D (2017) Dendritic GIRK Channels Gate the Integration Window, Plateau Potentials, and Induction of Synaptic Plasticity in Dorsal But Not Ventral CA1 Neurons. *J Neurosci* 37(14):3940-3955.
91. Brager DH, Akhavan AR, & Johnston D (2012) Impaired dendritic expression and plasticity of h-channels in the fmr1(-/y) mouse model of fragile X syndrome. *Cell reports* 1(3):225-233.
92. Kalmbach BE, Johnston D, & Brager DH (2015) Cell-Type Specific Channelopathies in the Prefrontal Cortex of the fmr1-/y Mouse Model of Fragile X Syndrome(1,2,3). *eNeuro* 2(6).
93. Arnold EC, McMurray C, Gray R, & Johnston D (2019) Epilepsy-Induced Reduction in HCN Channel Expression Contributes to an Increased Excitability in Dorsal, But Not Ventral, Hippocampal CA1 Neurons. *eNeuro* 6(2).

94. Das A & Narayanan R (2014) Active dendrites regulate spectral selectivity in location-dependent spike initiation dynamics of hippocampal model neurons. *J Neurosci* 34(4):1195-1211.
95. Das A & Narayanan R (2015) Active dendrites mediate stratified gamma-range coincidence detection in hippocampal model neurons. *J Physiol* 593(16):3549-3576.
96. Das A & Narayanan R (2017) Theta-frequency selectivity in the somatic spike triggered average of rat hippocampal pyramidal neurons is dependent on HCN channels. *Journal of neurophysiology* 118(4):2251-2266.
97. Fransen E, Alonso AA, Dickson CT, Magistretti J, & Hasselmo ME (2004) Ionic mechanisms in the generation of subthreshold oscillations and action potential clustering in entorhinal layer II stellate neurons. *Hippocampus* 14(3):368-384.
98. DiFrancesco D (2019) A Brief History of Pacemaking. *Front Physiol* 10:1599.
99. Ratte S, Hong S, De Schutter E, & Prescott SA (2013) Impact of neuronal properties on network coding: roles of spike initiation dynamics and robust synchrony transfer. *Neuron* 78(5):758-772.
100. Williams SR & Stuart GJ (2000) Site independence of EPSP time course is mediated by dendritic I(h) in neocortical pyramidal neurons. *Journal of neurophysiology* 83(5):3177-3182.
101. Magee JC (1998) Dendritic hyperpolarization-activated currents modify the integrative properties of hippocampal CA1 pyramidal neurons. *J Neurosci* 18(19):7613-7624.
102. Magee JC (1999) Dendritic Ih normalizes temporal summation in hippocampal CA1 neurons. *Nat Neurosci* 2(9):848.
103. Magee JC (2000) Dendritic integration of excitatory synaptic input. *Nature reviews. Neuroscience* 1(3):181-190.
104. Nolan MF, Malleret G, Dudman JT, Buhl DL, Santoro B, Gibbs E, Vronskaya S, Buzsaki G, Siegelbaum SA, Kandel ER, & Morozov A (2004) A behavioral role for dendritic integration: HCN1 channels constrain spatial memory and plasticity at inputs to distal dendrites of CA1 pyramidal neurons. *Cell* 119(5):719-732.
105. Vaidya SP & Johnston D (2013) Temporal synchrony and gamma-to-theta power conversion in the dendrites of CA1 pyramidal neurons. *Nat Neurosci* 16(12):1812-1820.
106. Sinha M & Narayanan R (2015) HCN channels enhance spike phase coherence and regulate the phase of spikes and LFPs in the theta-frequency range. *Proc Natl Acad Sci U S A* 112(17):E2207-2216.
107. Ness TV, Remme MWH, & Einevoll GT (2016) Active subthreshold dendritic conductances shape the local field potential. *J Physiol-London* 594(13):3809-3825.
108. Ness TV, Remme MWH, & Einevoll GT (2018) h-Type Membrane Current Shapes the Local Field Potential from Populations of Pyramidal Neurons. *J Neurosci* 38(26):6011-6024.
109. Fan Y, Fricker D, Brager DH, Chen X, Lu HC, Chitwood RA, & Johnston D (2005) Activity-dependent decrease of excitability in rat hippocampal neurons through increases in I(h). *Nat Neurosci* 8(11):1542-1551.
110. Ashhad S, Johnston D, & Narayanan R (2015) Activation of InsP3 receptors is sufficient for inducing graded intrinsic plasticity in rat hippocampal pyramidal neurons. *Journal of neurophysiology* 113(7):2002-2013.

111. Honnuraiah S & Narayanan R (2013) A calcium-dependent plasticity rule for HCN channels maintains activity homeostasis and stable synaptic learning. *PloS one* 8(2):e55590.
112. Narayanan R & Johnston D (2010) The h current is a candidate mechanism for regulating the sliding modification threshold in a BCM-like synaptic learning rule. *Journal of neurophysiology* 104(2):1020-1033.
113. Anirudhan A & Narayanan R (2015) Analogous synaptic plasticity profiles emerge from disparate channel combinations. *J Neurosci* 35(11):4691-4705.
114. Giocomo LM, Hussaini SA, Zheng F, Kandel ER, Moser MB, & Moser EI (2011) Grid cells use HCN1 channels for spatial scaling. *Cell* 147(5):1159-1170.
115. Hafting T, Fyhn M, Bonnevie T, Moser MB, & Moser EI (2008) Hippocampus-independent phase precession in entorhinal grid cells. *Nature* 453(7199):1248-1252.
116. Rowland DC, Roudi Y, Moser MB, & Moser EI (2016) Ten Years of Grid Cells. *Annu Rev Neurosci* 39:19-40.
117. Schmidt-Hieber C, Toleikyte G, Aitchison L, Roth A, Clark BA, Branco T, & Hausser M (2017) Active dendritic integration as a mechanism for robust and precise grid cell firing. *Nat Neurosci* 20(8):1114-1121.
118. Sreenivasan S & Fiete I (2011) Grid cells generate an analog error-correcting code for singularly precise neural computation. *Nat Neurosci* 14(10):1330-1337.
119. Welinder PE, Burak Y, & Fiete IR (2008) Grid cells: the position code, neural network models of activity, and the problem of learning. *Hippocampus* 18(12):1283-1300.
120. Burak Y & Fiete I (2006) Do we understand the emergent dynamics of grid cell activity? *J Neurosci* 26(37):9352-9354; discussion 9354.
121. Giocomo LM, Moser MB, & Moser EI (2011) Computational models of grid cells. *Neuron* 71(4):589-603.
122. O'Keefe J & Burgess N (2005) Dual phase and rate coding in hippocampal place cells: theoretical significance and relationship to entorhinal grid cells. *Hippocampus* 15(7):853-866.
123. Burgess N, Barry C, & O'Keefe J (2007) An oscillatory interference model of grid cell firing. *Hippocampus* 17(9):801-812.
124. Jeewajee A, Barry C, O'Keefe J, & Burgess N (2008) Grid cells and theta as oscillatory interference: electrophysiological data from freely moving rats. *Hippocampus* 18(12):1175-1185.
125. Bush D & Burgess N (2014) A hybrid oscillatory interference/continuous attractor network model of grid cell firing. *J Neurosci* 34(14):5065-5079.
126. Navratilova Z, Giocomo LM, Fellous JM, Hasselmo ME, & McNaughton BL (2012) Phase precession and variable spatial scaling in a periodic attractor map model of medial entorhinal grid cells with realistic after-spike dynamics. *Hippocampus* 22(4):772-789.
127. Burgess N & O'Keefe J (2011) Models of place and grid cell firing and theta rhythmicity. *Current opinion in neurobiology* 21(5):734-744.
128. Johnston D & Narayanan R (2008) Active dendrites: colorful wings of the mysterious butterflies. *Trends Neurosci* 31(6):309-316.
129. Narayanan R & Johnston D (2012) Functional maps within a single neuron. *Journal of neurophysiology* 108(9):2343-2351.
130. Stuart GJ & Spruston N (2015) Dendritic integration: 60 years of progress. *Nat Neurosci* 18(12):1713-1721.

131. Branco T & Hausser M (2011) Synaptic integration gradients in single cortical pyramidal cell dendrites. *Neuron* 69(5):885-892.
132. R Core Team (2013) *R: A Language and Environment for Statistical Computing* (R Foundation for Statistical Computing (http://www.R-project.org), Vienna, Austria).

FIGURE LEGENDS

Figure 1: A fast virtual trajectory developed for simulating rodent run in a two-dimensional circular arena elicits grid-cell activity in a continuous attractor network (CAN) model. (*A*) *Panels within rectangular box*: simulation of a CAN model (60×60 neural network) using a 589 s-long real trajectory from a rat (60) yielded grid cell activity. *Other panels*: A virtual trajectory (see Methods) was employed for simulating a CAN model (60×60 neural network) for different time points. The emergent activity patterns for 9 different run times (T_{run}) of the virtual animal are shown to yield grid cell activity. Top subpanels show color-coded neural activity through the trajectory, and bottom subpanels represent a smoothened spatial profile of neuronal activity shown in the respective top subpanels. (*B*) Pearson's correlation coefficient between the spatial autocorrelation of rate maps using the real trajectory and the spatial autocorrelation of rate maps from the virtual trajectory for the 9 different values of T_{run}, plotted for all neurons (n = 3600) in the network.

Figure 2: Biologically prevalent network heterogeneities disrupt the emergence of grid cell activity in CAN models. (*A*) Intrinsic heterogeneity was introduced by setting the integration time constant (τ) of each neuron to a random value picked from a uniform distribution, whose range was increased to enhance the degree of intrinsic heterogeneity. The values of τ for the 3600 neurons in the 60×60 CAN network are shown for 5 degrees of intrinsic heterogeneity. (*B*) Afferent heterogeneity was introduced by setting the velocity-scaling factor (α) of each neuron to a random value picked from a uniform distribution, whose range was increased to enhance the degree of intrinsic heterogeneity. The values of α for the 3600 neurons are shown for 5 degrees of afferent heterogeneity. (*C*) Synaptic heterogeneity was introduced as an additive jitter to the intra-network Mexican hat connectivity matrix, with the magnitude of additive jitter defining the degree of synaptic heterogeneity. Plotted are the root mean square error (RMSE) values computed between the connectivity matrix of "no jitter" case and that for different degrees of synaptic heterogeneities, across all synapses. (*D*) Illustration of a one-dimensional slice of synaptic strengths with different degrees of heterogeneity, depicted for Mexican-hat connectivity of a given cell to 60 other cells in the network. (*E*) *Top left*, virtual trajectory employed to obtain activity patterns of the CAN network. *Top center*, Example rate maps of grid cell activity in a homogeneous CAN network. *Top right*, smoothed version of the rate map. *Rows 2–4*: smoothed version of rate maps obtained from CAN networks endowed with 5 different

degrees (increasing left to right) of disparate forms (*Row 2*: intrinsic; *Row 3*: afferent; *Row 4*: synaptic; and *Row 5*: all three heterogeneities together) of heterogeneities. (*F*) Percentage change in the grid score of individual neurons (n=3600) in networks endowed with the four forms and five degrees of heterogeneities, compared to the grid score of respective neurons in the homogeneous network.

Figure 3: Quantification of the disruption in grid-cell activity induced by different forms of network heterogeneities in the CAN model. Grid cell activity of individual neurons in the network was quantified by 8 different measurements, for CAN models endowed independently with intrinsic, afferent or synaptic heterogeneities or a combination of all three heterogeneities. (*A–G*) Depicted are percentage changes in each of average firing rate (*A*), peak firing rate (*B*), mean size (*C*), number (*D*), average spacing (*E*), information rate (*F*) and sparsity (*G*) for individual neurons (n=3600) in networks endowed with distinct forms of heterogeneities, compared to the grid score of respective neurons in the homogeneous network. (*H*) Grid score of individual cells (n=3600) in the network plotted as functions of integration time constant (τ), velocity modulation factor (α) and root mean square error (RMSE) between the connectivity matrices of the homogeneous and the heterogeneous CAN models. Different colors specify different degrees of heterogeneity. The three plots with reference to τ, α and RMSE are from networks endowed with intrinsic, afferent and synaptic heterogeneity, respectively.

Figure 4: Incorporation of biological heterogeneities predominantly altered neural activity in low frequencies. (*A–H*) *Left,* Magnitude spectra of temporal activity patterns of five example neurons residing in a homogeneous network (HN) or in networks with different forms and degrees of heterogeneities. *Right*, Normalized variance of the differences between the magnitude spectra of temporal activity of neurons in homogeneous *vs.* heterogeneous networks, across different forms and degrees of heterogeneities, plotted as a function of frequency.

Figure 5: Incorporation of an additional high pass filter into neuronal dynamics introduces resonance in individual rate-based neurons. (*A*) Responses of neurons with low-pass (integrator; blue), high-pass (black) and band-pass (resonator; red) filtering structures to a chirp stimulus (top). (*B*) Response magnitude of an integrator neuron (low-

pass filter) as a function of input frequency, derived from response to the chirp stimulus. (*C*) Response magnitude of a resonator neuron (band-pass filter; red) as a function of input frequency, derived from response to the chirp stimulus, shown to emerge as a combination of low- (blue) and high-pass (black) filters. f_R represents resonance frequency. (*D–E*) Tuning resonance frequency by altering the low-pass filter characteristics. Response magnitudes of 3 different resonating neurons with identical HPF exponent (ε=0.3), but with different integrator time constants (τ), plotted as functions of frequency (*D*). Resonance frequency can be tuned by adjusting τ for different fixed values of ε, with an increase in τ yielding a reduction in f_R (*E*). (*F–G*) Tuning resonance frequency by altering the high-pass filter characteristics. Response magnitudes of 3 different resonating neurons with identical τ (=10 ms), but with different values for ε, plotted as functions of frequency (*F*). Resonance frequency can be tuned by adjusting ε for different fixed values of τ, with an increase in ε yielding an increase in f_R (*G*).

Figure 6: Impact of neuronal resonance, introduced by altering low-pass filter characteristics, on grid-cell activity in a homogeneous CAN model. (*A*) Example rate maps of grid cell activity from a homogeneous CAN model with integrator neurons modeled with different values for integration time constants (τ). (*B*) Example rate maps of grid cell activity from a homogeneous CAN model with resonator neurons modeled with different τ values. (*C–D*) Grid score (*C*), average spacing (*D*), mean size (*E*) and number (*F*) of grid fields in the arena for all neurons (*n*=3600) in homogeneous CAN models with integrator (blue) or resonator (red) neurons, modeled with different τ values. The HPF exponent ε was set to 0.3 for all resonator neuronal models.

Figure 7: Impact of neuronal resonance, introduced by altering high-pass filter characteristics, on grid-cell activity in a homogeneous CAN model. (*A*) Example rate maps of grid cell activity from a homogeneous CAN model with integrator neurons (*Column 1*) or resonator neurons (*Columns 2–6*) modeled with different values of the HPF exponent (ε). (*B*) Comparing 8 metrics of grid cell activity for all the neurons (*n*=3600) in CAN models with integrator (blue) or resonator (green) neurons. CAN models with resonator neurons were simulated for different ε values. τ = 10 ms for all networks depicted in this figure.

Figure 8: Neuronal resonance stabilizes grid-cell activity in heterogeneous CAN models. (*A*) Example rate maps of grid-cell activity in homogeneous (*Top left*) and heterogeneous CAN models, endowed with resonating neurons, across different degrees of heterogeneities. (*B–I*) Percentage changes in grid score (*B*), average spacing (*C*), peak firing rate (*D*), average firing rate (*E*), number (*F*), mean size (*G*), information rate (*H*), and sparsity (*I*) of grid field for all neurons (n=3600) in the heterogeneous CAN network, plotted for 5 degrees of heterogeneities (D1–D5), compared with respective neurons in the homogeneous resonator network. All three forms of heterogeneities were incorporated together into the network. ε =0.3 and τ = 10 ms for all networks depicted in this figure.

Figure 9: Intrinsically resonating neurons suppressed heterogeneity-induced variability in low-frequency perturbations caused by the incorporation of biological heterogeneities. (*A*) Normalized variance of the differences between the magnitude spectra of temporal activity in neurons of homogeneous *vs.* heterogeneous networks, across different degrees of all three forms of heterogeneities expressed together, plotted as a function of frequency. (*B*) Area under the curve (AUC) of the normalized variance plots shown in Fig. 4*H* (for the integrator network) and panel *A* (for the resonator network) showing the variance to be lower in resonator networks compared to integrator networks. The inset shows the total AUC across all frequencies for the integrator *vs*. the resonator networks as a function of the degree of heterogeneities. (*C*) Difference between the normalized magnitude spectra of neural temporal activity patterns for integrator and resonator neurons in CAN models. Solid lines depict the mean and shaded area depicts the standard deviations, across all 3600 neurons.

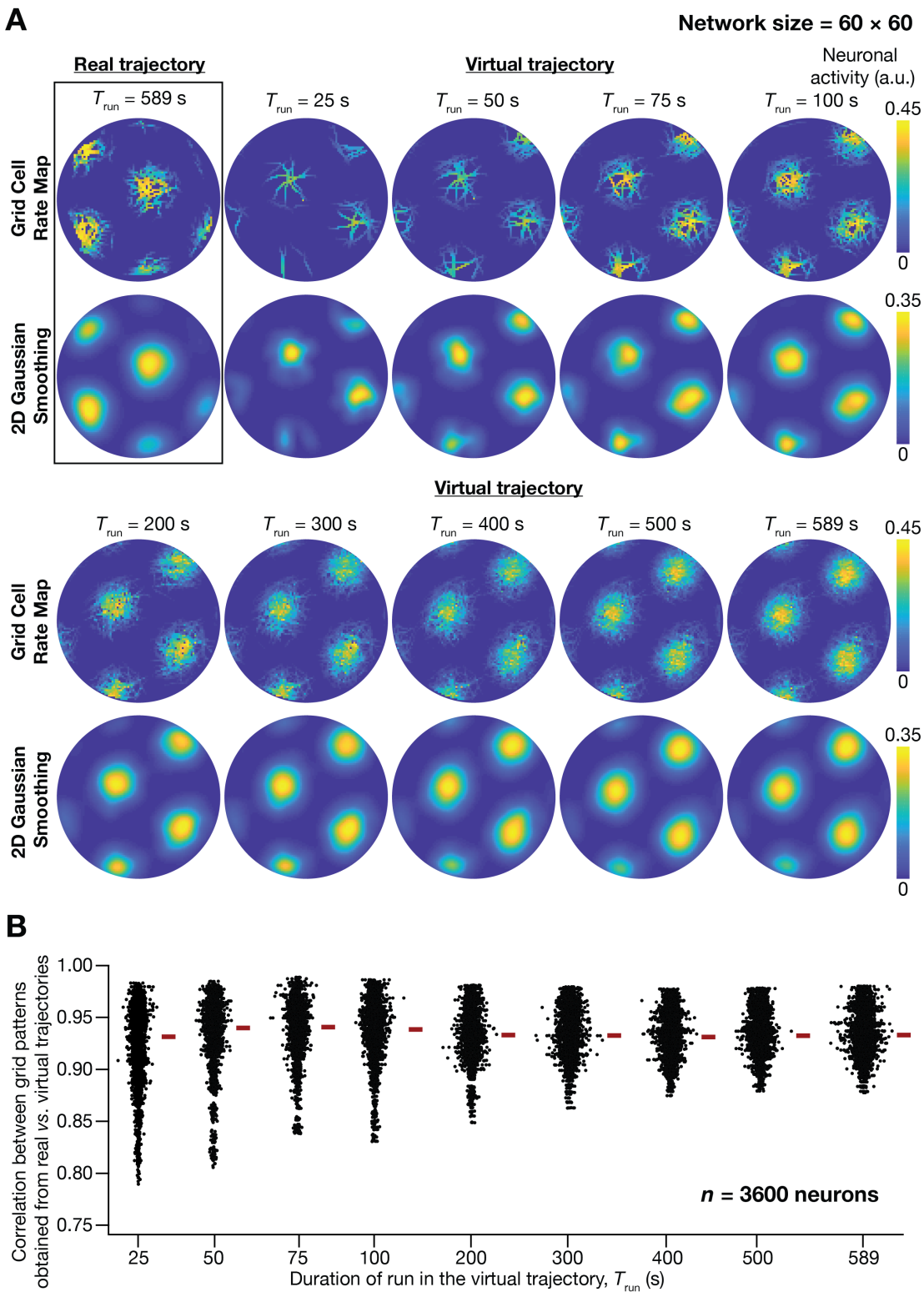

Mittal and Narayanan, Figure 1

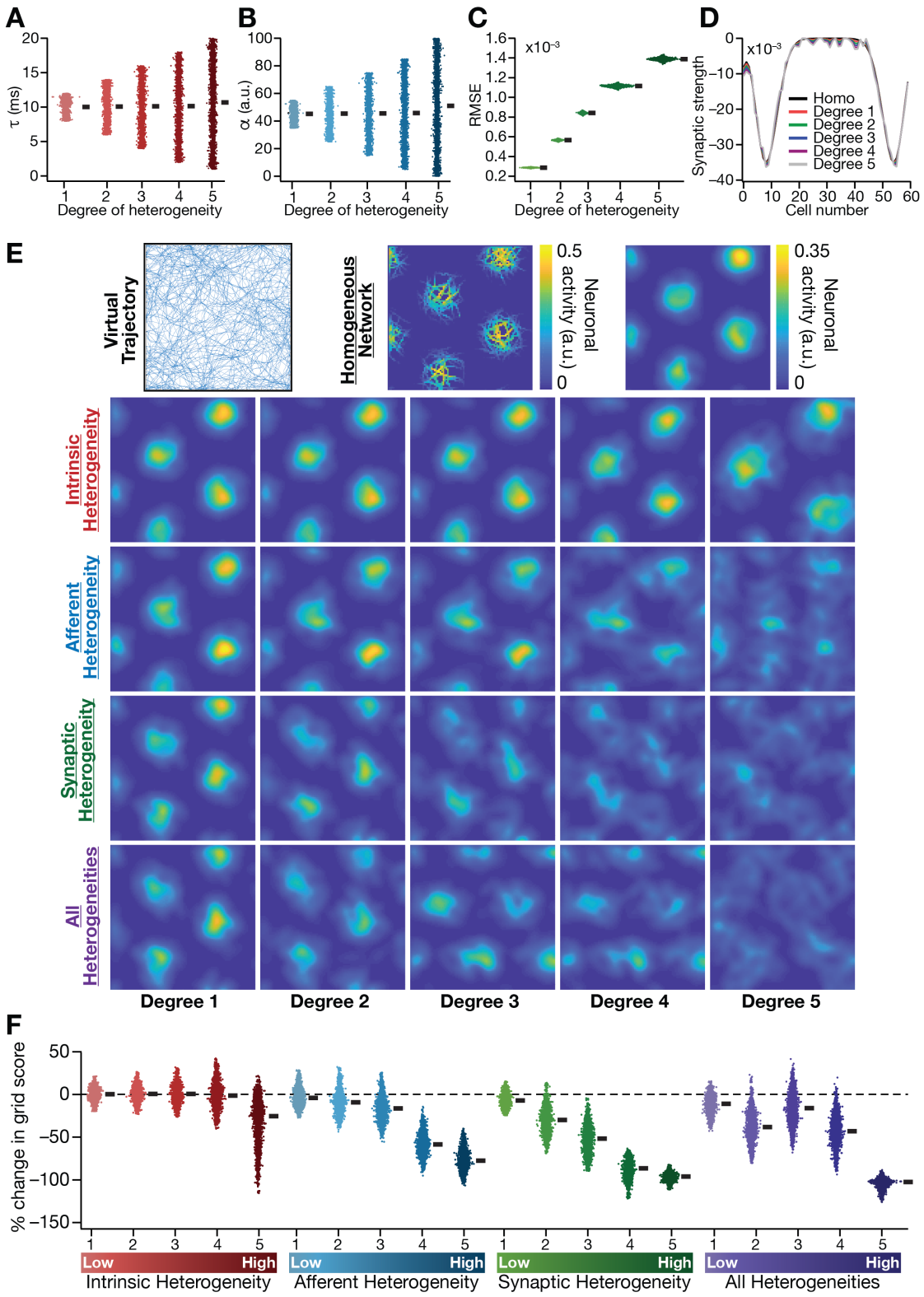

Mittal and Narayanan, Figure 2

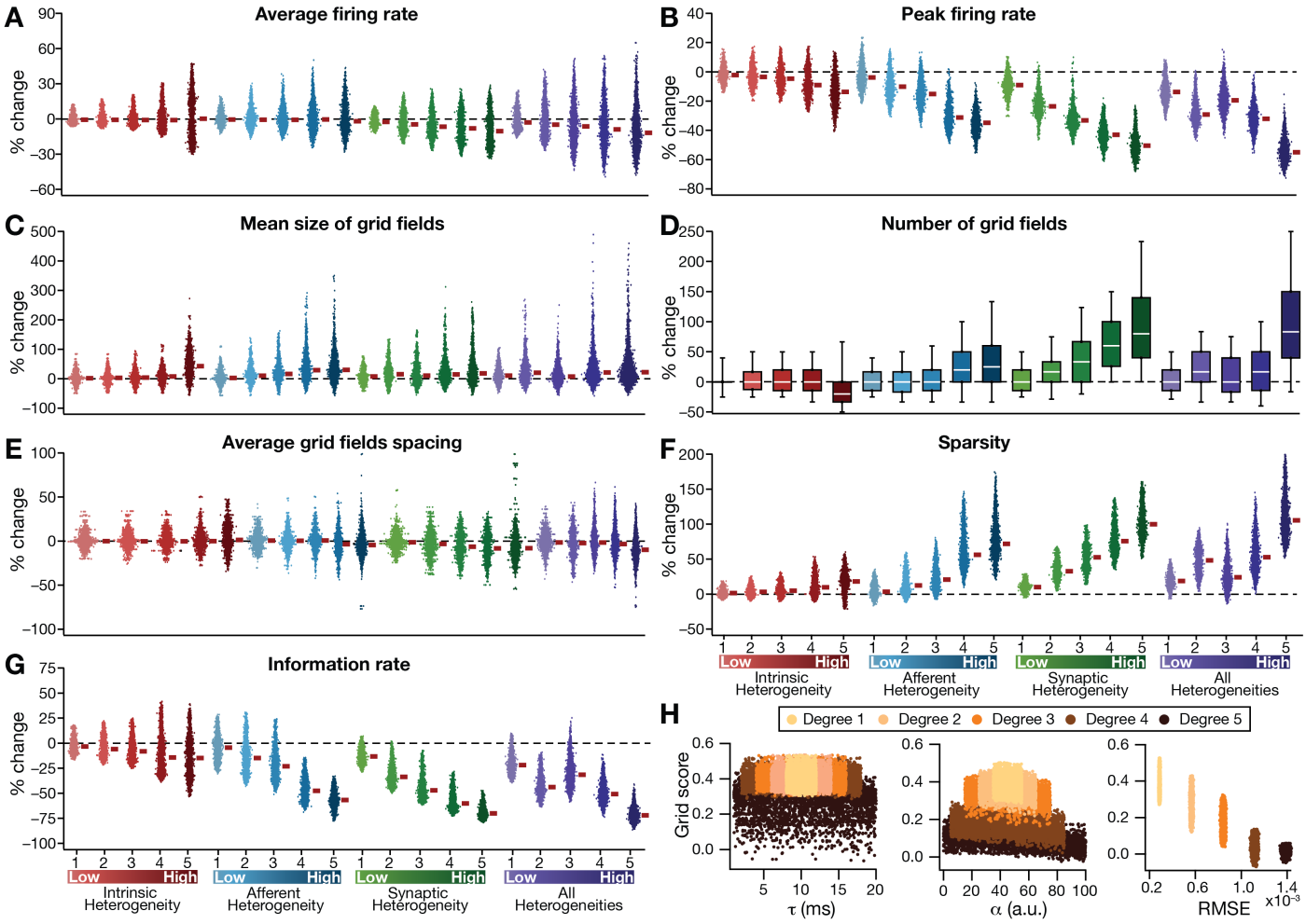

Mittal and Narayanan, Figure 3

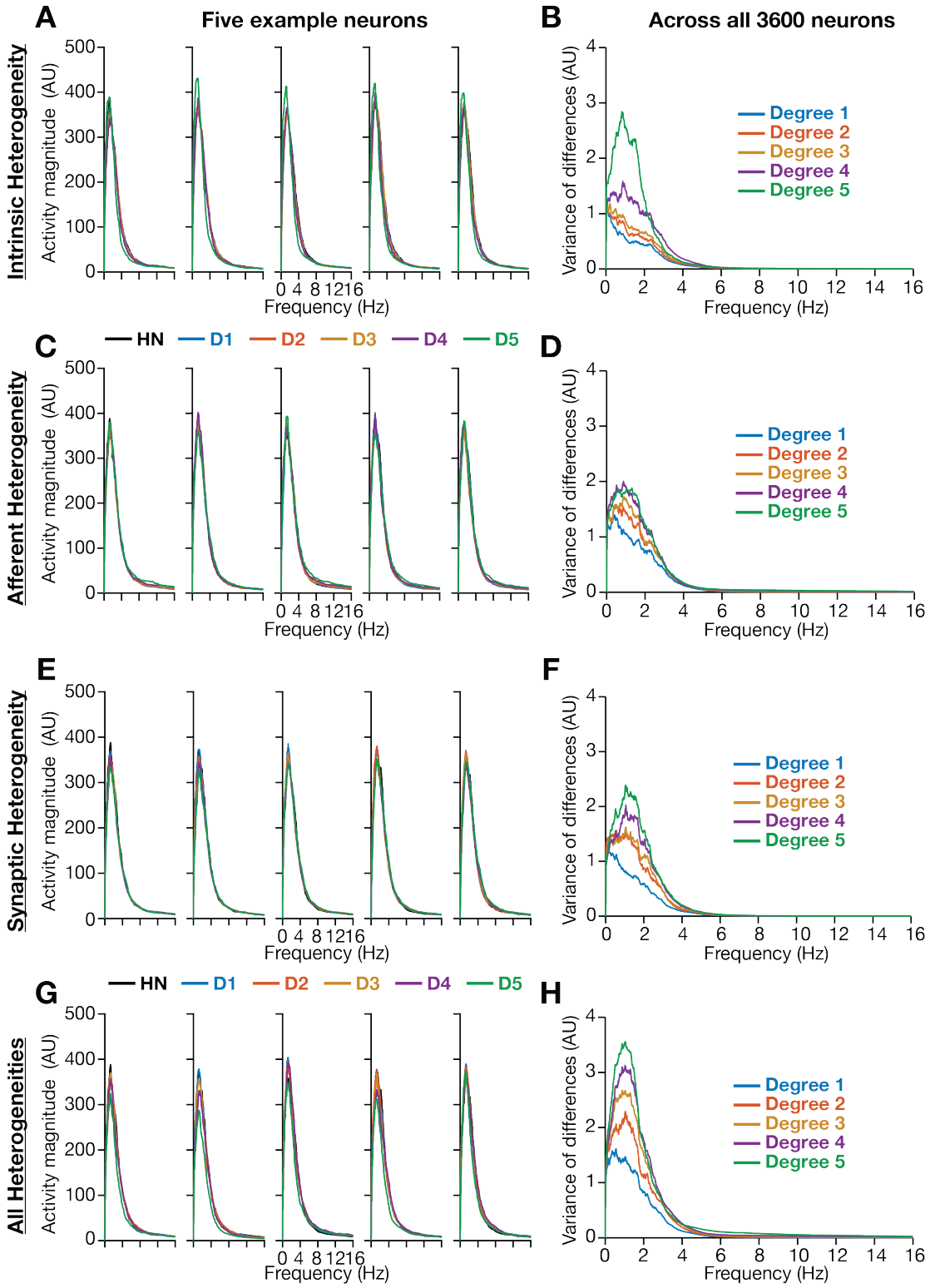

Mittal and Narayanan, Figure 4

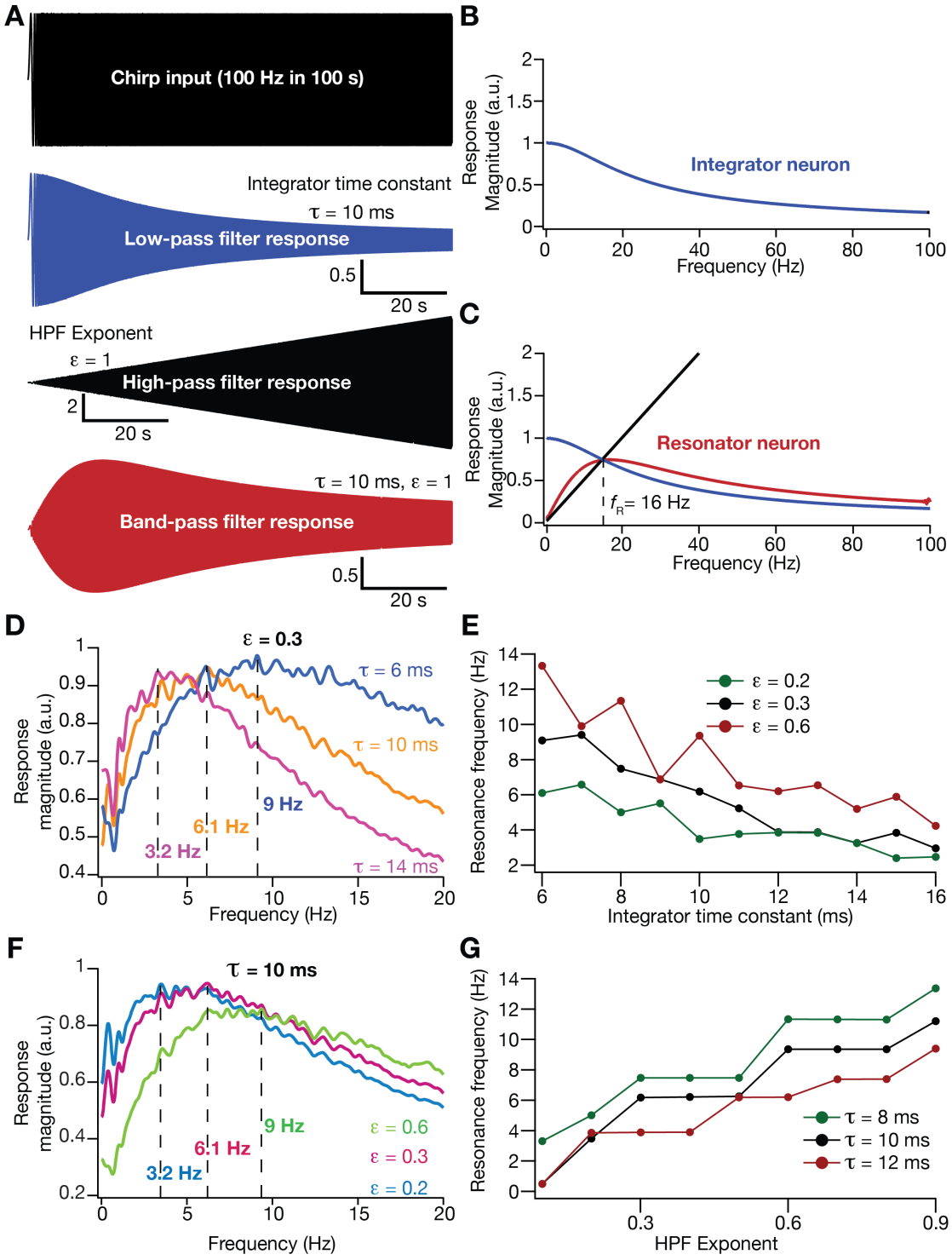

Mittal and Narayanan, Figure 5

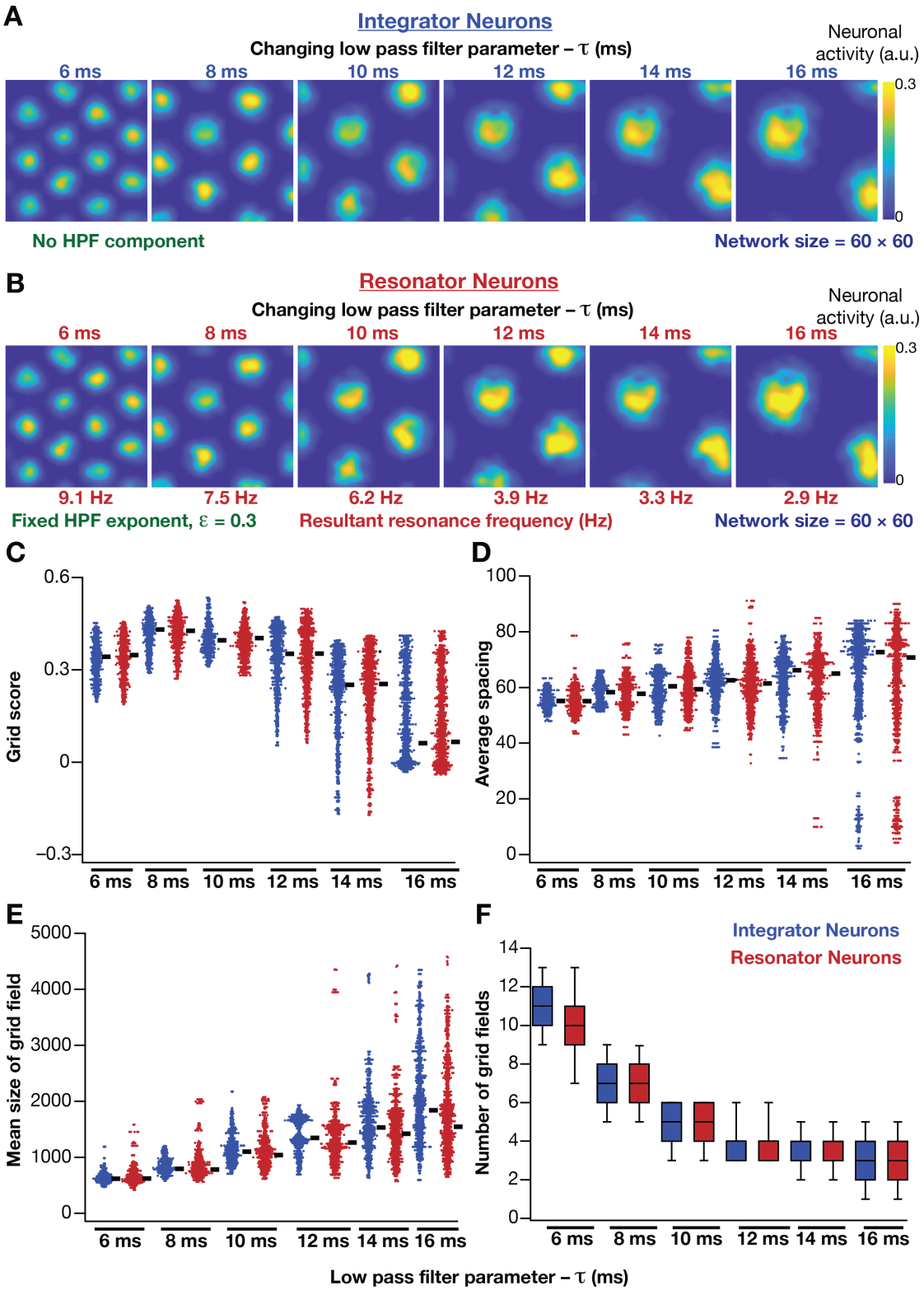

Mittal and Narayanan, Figure 6

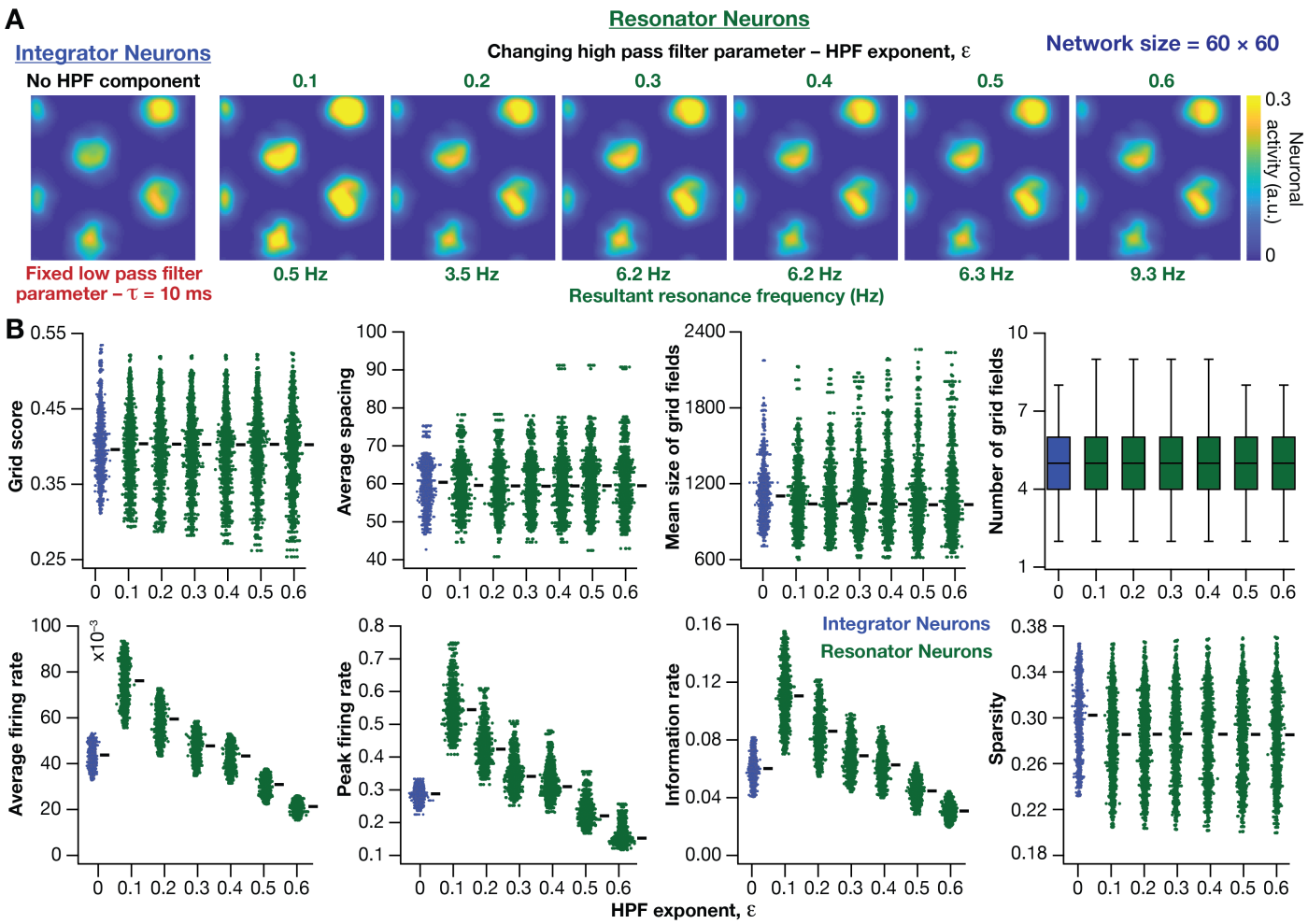

Mittal and Narayanan, Figure 7

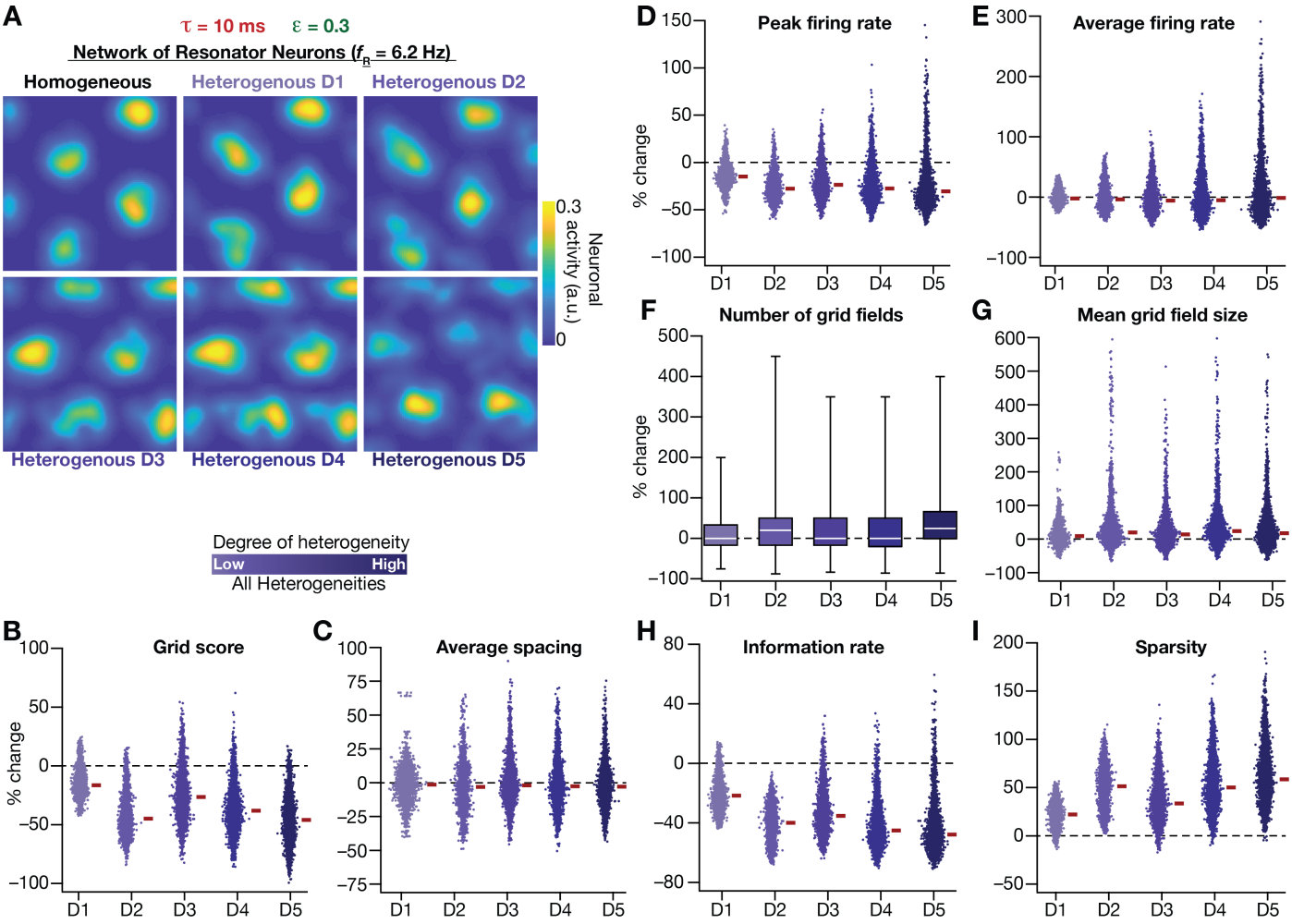

Mittal and Narayanan, Figure 8

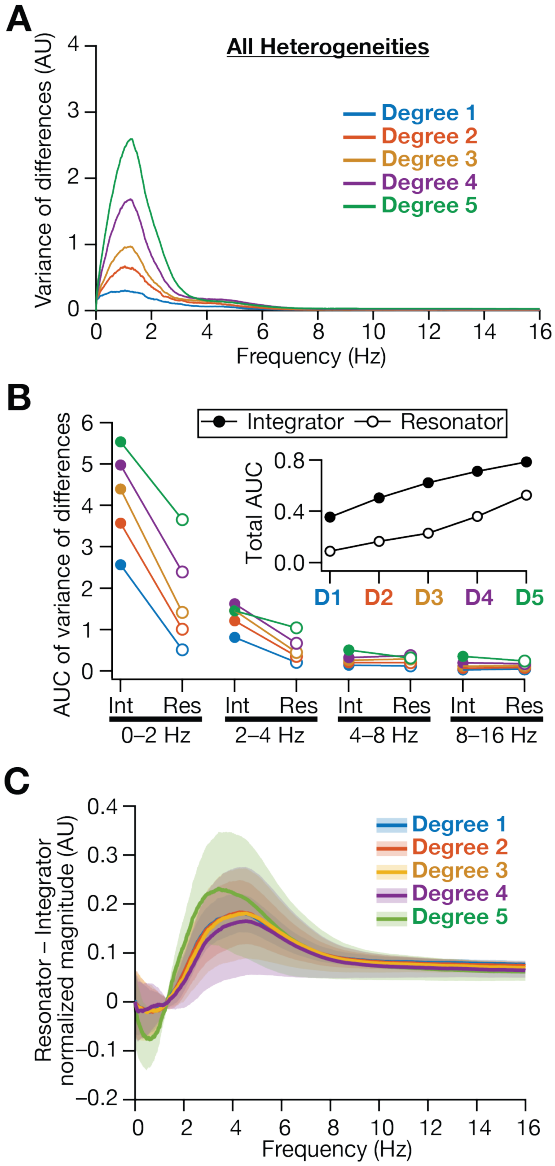

Mittal and Narayanan, Figure 9